Wave propagation in three-phase porous piezoelectric media: theory and simulation

Zhi-Xiang Sun(孙智翔)[1,2], Yin-Qiu Zhou(周吟秋)[1,2,*], Xiu-Ming Wang(王秀明)[1,2], Lin Liu(刘琳)[1,2], Xiao He(何晓)[1,2], and Yong-Hao Lu(鲁永灏)[1,2]

[1]Institute of Acoustics, Chinese Academy of Sciences, Beijing 100190, China

[2]University of Chinese Academy of Sciences, Beijing 100049, China

July 31, 2026

Abstract

Acoustic-wave propagation in multiphase porous piezoelectric media is closely related to optimizing piezoelectric composite transducers and to the remodelling and regeneration of cancellous bone. Most existing wave theories, however, treat a two-phase system of one piezoelectric skeleton and one fluid, whereas classical three-phase models seldom include both anisotropy and piezoelectric coupling. This study investigates, both theoretically and numerically, elastic wave propagation in a three-phase porous piezoelectric medium. The medium comprises a transversely isotropic piezoelectric skeleton, a compressible pore fluid, and a non-piezoelectric filling solid, with piezoelectricity confined to the skeleton. The governing equations couple a Biot-type three-phase momentum balance with the piezoelectric constitutive relations. Introducing a plane-wave ansatz reduces the problem to a complex Christoffel system, which yields the phase velocity, group velocity, and attenuation of seven body-wave modes: three quasi-compressional, two quasi-shear, and two horizontally polarized shear (SH) waves. For wavefield simulation, a two-dimensional electromechanically coupled staggered-grid finite-difference time-domain algorithm is developed, together with a coupled electromechanical perfectly matched layer for the poroelastic and piezoelectric fields. The simulated arrival times agree with the Christoffel predictions to within 1%, and, in the reduced single-solid, single-fluid limit, the scheme is benchmarked against a commercial finite-element poroelastic solution. The results show that piezoelectric coupling anisotropically stiffens the skeleton-borne quasi-compressional and quasi-shear waves, while leaving the SH waves unchanged. Interphase friction selectively attenuates the slow modes: the friction between skeleton and pore fluid predominantly damps the fluid-borne slow wave, whereas that between the two solids attenuates the filling-solid-borne waves.

Keywords: three-phase porous piezoelectric media, acoustic wave propagation, Christoffel equation, finite-difference time-domain method

PACS: 43.20.+g, 77.65.-j

*Corresponding author. E-mail: zhouyinqiu@mail.ioa.ac.cn

1. Introduction

Porous piezoelectric media are heterogeneous solids in which a solid skeleton and one or more pore-filling phases form a piezoelectrically active whole; familiar examples include porous piezoelectric ceramics, ceramic–polymer piezocomposites, and biological tissues such as bone [1,2]. The acoustics of such media is a long-standing problem of both fundamental and practical importance: it underpins the acoustic design of porous piezoelectric composites and their transducers [3], while in bone the intrinsic piezoelectricity is implicated in mechanotransduction and remodelling and is routinely probed by quantitative ultrasound [4,5]. In many natural and engineered settings, however, the pore space holds not a fluid alone but a fluid together with a second solid, for example a polymer infill in a piezocomposite or a hydrate or ice phase in a fluid-saturated host, so that the medium becomes genuinely three-phase, with two solids and one fluid. Body-wave propagation, anisotropy, and dissipation are then governed jointly by the electromechanical coupling of the skeleton and the multiphase filling of the pores.

Any treatment of such media builds on classical poroelasticity. Biot established the mechanics of wave propagation in a fluid-saturated porous solid, predicting two compressional waves and one shear wave: a fast P wave, in which the skeleton and pore fluid move in phase, and a diffusive slow P wave, arising from their out-of-phase motion [6–8]. Long regarded as a theoretical prediction, the slow wave was later observed by Plona [9], confirming a framework that now underpins poroelastic acoustics in petroleum exploration, geomechanics, and ultrasonics [10]. Biot's formulation, however, treats a single skeleton saturated by a single fluid, with no electromechanical coupling in its constitutive relations.

Extending poroelasticity to a piezoelectric skeleton, Vashishth and Gupta coupled Biot's theory with the piezoelectric constitutive law and derived the Christoffel equation for transversely isotropic (6mm) porous piezoelectric materials, predicting four bulk modes—two quasi-dilatational and two quasi-shear—with complex velocities [11]. Sharma isolated the stiffening contribution of the electromechanical coupling to these velocities [12], while later studies clarified the symmetry-allowed decoupling of certain plane-wave subsystems [13] and treated interface reflection and transmission [14] and guided waves in graded structures [15]. A complementary homogenization route has derived effective piezo-poroelastic constitutive laws for fluid-saturated piezoelectric microstructures, including the electric-field–pore-pressure coupling [16]. Throughout, however, these studies assume a single piezoelectric skeleton saturated by one fluid; the two-solid, one-fluid case, in which a non-piezoelectric solid occupies part of the pore space and adds inertial, frictional, and stiffness couplings, lies outside their scope.

A separate line of research treats porous media with more than one solid constituent. Leclaire *et al.* extended Biot's theory to frozen porous media, treating the mineral skeleton and pore ice as two elastically coupled solids sharing a common fluid and predicting three compressional and two shear waves [17]. Carcione and Seriani recast this three-phase theory in a velocity–stress form suited to simulation and applied it to gas-hydrate-bearing sediments and partially frozen media [18,19]. Because pore-scale friction between the two solids controls the attenuation of the extra slow modes [20], a faithful description requires explicit interphase friction alongside inertial and stiffness coupling; recent staggered-grid finite-difference

implementations have simulated all five wave modes in such sediments and quantified how solid–solid friction and fluid viscosity regulate slow-wave attenuation [21,22]. A four-phase theory, in which the skeleton hosts a solid and two pore fluids, raises the count further, to four compressional and two shear waves [23]. These models, however, assume isotropic, non-piezoelectric constituents; none incorporates an anisotropic piezoelectric skeleton or its electromechanical coupling.

On the numerical side, the velocity–stress staggered-grid finite-difference time-domain (FDTD) method has become a standard tool for elastic and poroelastic wavefields, owing to its accuracy and natural treatment of heterogeneity [24,25]; for piezoelectric solids, anisotropic electromechanical finite-element and finite-difference formulations have long been available [26,27], including hybrid pseudospectral/finite-difference transducer models [28]. For the three-phase porous piezoelectric problem considered here, the difficulty lies less in the poroelastic and electric fields taken separately than in coupling them faithfully in the time domain: the common quasi-static shortcut of setting the electric-displacement rate to zero ties the electric field locally to the instantaneous strain and can introduce an artificial stiffening, whereas preserving the coupling requires solving a Poisson equation for the electric potential at every step. Open-domain simulation adds a second requirement, an effective absorbing boundary. The perfectly matched layer (PML) [29] has been adapted to anisotropic elastic [30], poroelastic [31], and, recently, piezoelectric [32] media, but to our knowledge no PML absorbs the skeleton, pore-fluid, and electric-potential fields of a three-phase piezo-poroelastic medium at once.

These two lines have developed largely in parallel. A three-phase medium whose load-bearing skeleton is an anisotropic piezoelectric solid falls outside both the two-phase porous piezoelectric theory and the isotropic, non-piezoelectric three-phase models, and no coupled time-domain wavefield simulation that advances the mechanical, pore-fluid, and electric fields together has been reported for it.

The present work, both theoretical and numerical, addresses this gap. We study acoustic wave propagation in a three-phase porous piezoelectric medium formed by a transversely isotropic (6mm) piezoelectric ceramic skeleton, an isotropic compressible pore fluid, and a non-piezoelectric filling solid such as hydrate, ice, or polymer, with piezoelectricity confined to the skeleton. Coupling the Biot-type momentum equations with the piezoelectric constitutive relations reduces the plane-wave problem to a complex Christoffel system that yields the phase velocity, group velocity, and attenuation of the compressional and shear branches as functions of propagation direction. For two-dimensional wavefield simulation in the sagittal plane, we develop a staggered-grid FDTD scheme that advances the velocity, electric-potential, and stress fields with the coupling kept intact, together with a coupled electromechanical PML that absorbs all three fields. The scheme is verified against the Christoffel arrival times and, in the reduced single-solid, single-fluid limit (filling solid removed, piezoelectric coupling off), cross-checked against a COMSOL poroelastic-wave benchmark and, in two further reduced cases, against published results. The validated tools then reveal how the piezoelectric coupling stiffens the skeleton-borne quasi-compressional and quasi-shear waves and how the interphase friction coefficients govern slow-mode attenuation.

The rest of this paper is organized as follows. Section 2 develops the governing equations, the plane-

wave Christoffel analysis, the staggered-grid FDTD scheme, and the coupled electromechanical PML. Section 3 presents the numerical results and their verification, and Section 4 concludes the paper.

2. Theory and numerical method

2.1. Governing equations

The three-phase medium studied here consists of a transversely isotropic piezoelectric ceramic skeleton of crystal class 6mm (phase 1), an isotropic compressible pore fluid (phase 2), and an isotropic non-piezoelectric filling solid (phase 3) such as hydrate, ice, or polymer, with the piezoelectric effect confined to the skeleton. A parenthesized superscript labels the phase, a subscript comma denotes spatial differentiation, an overdot denotes time differentiation, and repeated lowercase indices $i, j, k, l \in \{1, 2, 3\}$ are summed. The two solid phases are described by the strains $\varepsilon_{ij}^{(\alpha)} = \frac{1}{2}(u_{i,j}^{(\alpha)} + u_{j,i}^{(\alpha)})$ $(\alpha = 1, 3)$, and the pore fluid by the dilatation $\zeta = u_{k,k}^{(2)}$. The electric field is quasi-static, $E_k = -\Phi_{,k}$, because the electromagnetic wavelengths far exceed the acoustic ones.

The constitutive relations follow from a thermodynamic potential, constructed in the standard manner of linear piezoelectricity [33–35]. For an isothermal, reversible process, with piezoelectricity confined to the skeleton, the internal-energy density U of the three-phase aggregate per unit bulk volume changes as

$$\mathrm{d}U = \sigma_{ij}^{(1)}\,\mathrm{d}\varepsilon_{ij}^{(1)} + \sigma^{(2)}\,\mathrm{d}\zeta + \sigma_{ij}^{(3)}\,\mathrm{d}\varepsilon_{ij}^{(3)} + E_i\,\mathrm{d}D_i, \tag{1}$$

where $\sigma_{ij}^{(1)}$ and $\sigma_{ij}^{(3)}$ are the stresses of the two solid phases, $\sigma^{(2)}$ is the scalar fluid stress, and D_i is the electric displacement; the mechanical terms generalize the strain energy of two-phase [6] and three-phase [17] poroelasticity. Because the quasi-static problem prescribes the electric potential rather than the electric displacement, we pass to the electric-enthalpy density W by the Legendre transformation

$$W = U - E_i D_i, \qquad \mathrm{d}W = \sigma_{ij}^{(1)}\,\mathrm{d}\varepsilon_{ij}^{(1)} + \sigma^{(2)}\,\mathrm{d}\zeta + \sigma_{ij}^{(3)}\,\mathrm{d}\varepsilon_{ij}^{(3)} - D_i\,\mathrm{d}E_i. \tag{2}$$

In the linear theory, W is a quadratic form in the strain measures and the electric field. The pore fluid and the filling solid are isotropic and non-piezoelectric, so the electric field couples to the skeleton strain alone; the fluid-phase piezoelectric couplings retained in Ref. [11] are therefore absent here. The most general quadratic form consistent with these assumptions is

$$\begin{aligned} W \;=\; & \tfrac{1}{2}c_{ijkl}^{(11)}\varepsilon_{ij}^{(1)}\varepsilon_{kl}^{(1)} + \tfrac{1}{2}c_{ijkl}^{(33)}\varepsilon_{ij}^{(3)}\varepsilon_{kl}^{(3)} + \tfrac{1}{2}R\,\zeta^2 + c_{ijkl}^{(13)}\varepsilon_{ij}^{(1)}\varepsilon_{kl}^{(3)} \\ & + m_{ij}^{(12)}\varepsilon_{ij}^{(1)}\zeta + m_{ij}^{(32)}\varepsilon_{ij}^{(3)}\zeta - e_{kij}E_k\varepsilon_{ij}^{(1)} - \tfrac{1}{2}\xi_{ij}E_iE_j, \end{aligned} \tag{3}$$

where the material tensors carry their usual symmetries (in particular the major symmetry $c_{ijkl}^{(13)} = c_{klij}^{(13)}$). Equation (2) identifies the stresses and the electric displacement as the conjugate quantities

$$\sigma_{ij}^{(1)} = \frac{\partial W}{\partial \varepsilon_{ij}^{(1)}}, \qquad \sigma^{(2)} = \frac{\partial W}{\partial \zeta}, \qquad \sigma_{ij}^{(3)} = \frac{\partial W}{\partial \varepsilon_{ij}^{(3)}}, \qquad D_i = -\frac{\partial W}{\partial E_i}. \tag{4}$$

Carrying out the differentiation, with $E_k = -\Phi_{,k}$, the minor symmetries of c_{ijkl} and e_{kij} ($c_{ijkl}\varepsilon_{kl} = c_{ijkl}u_{k,l}$, $e_{ikl}\varepsilon_{kl} = e_{ikl}u_{k,l}$), and the symmetry of m_{ij}, gives the constitutive relations

$$\sigma_{ij}^{(1)} = c_{ijkl}^{(11)}u_{k,l}^{(1)} + m_{ij}^{(12)}u_{k,k}^{(2)} + c_{ijkl}^{(13)}u_{k,l}^{(3)} + e_{kij}\Phi_{,k}, \tag{5}$$

$$\sigma^{(2)} = m_{ij}^{(12)}u_{i,j}^{(1)} + R\,u_{k,k}^{(2)} + m_{ij}^{(32)}u_{i,j}^{(3)}, \tag{6}$$

$$\sigma_{ij}^{(3)} = c_{ijkl}^{(13)}u_{k,l}^{(1)} + m_{ij}^{(32)}u_{k,k}^{(2)} + c_{ijkl}^{(33)}u_{k,l}^{(3)}, \tag{7}$$

$$D_i = e_{ikl}u_{k,l}^{(1)} - \xi_{ij}\Phi_{,j}, \tag{8}$$

where $u_i^{(\alpha)}$ are the phase displacements; $c_{ijkl}^{(11)}$, $c_{ijkl}^{(33)}$, and $c_{ijkl}^{(13)}$ the skeleton, filling-solid, and solid–solid coupling stiffnesses; $m_{ij}^{(12)}$ and $m_{ij}^{(32)}$ the solid–fluid couplings; R the effective fluid modulus; and e_{kij} and ξ_{ij} the piezoelectric and dielectric constants of the skeleton. Here ξ_{ij} is the clamped, or constant-strain, permittivity, since Eq. (8) gives $\xi_{ij} = \partial D_i/\partial E_j$ at fixed skeleton strain, with $E_j = -\Phi_{,j}$. Because W is an energy per unit bulk volume, $\sigma^{(2)}$ is a partial stress rather than the pressure within the fluid: it is the force per unit area of the bulk medium carried by the pore fluid, and is related to the pore pressure p_f of the usual Biot notation by $\sigma^{(2)} = -\phi_2 p_\mathrm{f}$, where ϕ_2 is the volume fraction of the pore fluid. The minus sign follows from the convention that stresses are positive in tension whereas p_f is positive in compression. Setting $e_{kij} = 0$ decouples the electric field and reduces Eqs. (5)–(7) to the constitutive relations of three-phase poroelasticity [17,18,21]; removing the filling solid instead recovers the porous piezoelectric medium of Vashishth and Gupta [11] in the limit where their fluid-phase piezoelectric and dielectric couplings are dropped.

The equations of motion follow from a variational principle. The kinetic-energy density and the Rayleigh dissipation function are

$$K = \tfrac{1}{2}\sum_{\alpha,\beta=1}^{3}\rho_{ik}^{\alpha\beta}\dot{u}_i^{(\alpha)}\dot{u}_k^{(\beta)}, \qquad \mathcal{R} = \tfrac{1}{2}\sum_{(\alpha,\beta)}b_{ik}^{\alpha\beta}\big(\dot{u}_i^{(\alpha)} - \dot{u}_i^{(\beta)}\big)\big(\dot{u}_k^{(\alpha)} - \dot{u}_k^{(\beta)}\big), \tag{9}$$

where $\rho_{ik}^{\alpha\beta}$ are the symmetric density tensors and $b_{ik}^{\alpha\beta}$ the friction tensors; the pair sum runs over $(1,2)$, $(1,3)$, and $(2,3)$. The symmetry $\rho_{ik}^{\alpha\beta} = \rho_{ik}^{\beta\alpha}$ leaves six independent density coefficients, three phase inertias and three inertial couplings, against the three of Biot's fluid–solid theory, while the three contacting pairs contribute three friction coefficients against its one. How the values of these coefficients are determined is set out in Subsection 2.2 for the friction tensors and in Appendix B for the density tensors. The extended Hamilton's principle in Lagrange–d'Alembert form, which accounts for the Rayleigh dissipation and the virtual work of the surface loads, requires the total virtual work to vanish:

$$\delta\int_{t_0}^{t_1}\int_V (K - W)\,\mathrm{d}V\,\mathrm{d}t + \int_{t_0}^{t_1}\Bigg[\int_S\Big(\sum_{\alpha=1}^{3}t_i^{(\alpha)}\delta u_i^{(\alpha)} + q_s\delta\Phi\Big)\mathrm{d}S - \int_V\sum_{\alpha=1}^{3}\frac{\partial\mathcal{R}}{\partial\dot{u}_i^{(\alpha)}}\delta u_i^{(\alpha)}\,\mathrm{d}V\Bigg]\mathrm{d}t = 0, \tag{10}$$

where $t_i^{(\alpha)}$ are the surface tractions of the three phases and q_s is the surface charge density. Collecting the

independent volume variations gives

$$\begin{aligned}
\sigma^{(1)}_{ij,j} &= \sum_{\beta=1}^{3} \rho^{1\beta}_{ik}\ddot{u}^{(\beta)}_k + \frac{\partial \mathcal{R}}{\partial \dot{u}^{(1)}_i}, \\
\sigma^{(2)}_{,i} &= \sum_{\beta=1}^{3} \rho^{2\beta}_{ik}\ddot{u}^{(\beta)}_k + \frac{\partial \mathcal{R}}{\partial \dot{u}^{(2)}_i}, \\
\sigma^{(3)}_{ij,j} &= \sum_{\beta=1}^{3} \rho^{3\beta}_{ik}\ddot{u}^{(\beta)}_k + \frac{\partial \mathcal{R}}{\partial \dot{u}^{(3)}_i}.
\end{aligned} \tag{11}$$

The surface integral yields the natural mechanical and electrical boundary conditions, which are not listed here because only the bulk equations are needed. The fluid equation involves the gradient $\sigma^{(2)}_{,i}$ because W depends on $u^{(2)}_i$ only through ζ. Differentiating $\mathcal{R}$ with respect to the two velocities of each contacting pair gives equal and opposite friction forces on the two phases, consistent with Newton's third law, and the equations of motion read

$$\begin{aligned}
\sigma^{(1)}_{ij,j} &= \rho^{11}_{ik}\ddot{u}^{(1)}_k + \rho^{12}_{ik}\ddot{u}^{(2)}_k + \rho^{13}_{ik}\ddot{u}^{(3)}_k \\
&\quad + b^{12}_{ik}(\dot{u}^{(1)}_k - \dot{u}^{(2)}_k) + b^{13}_{ik}(\dot{u}^{(1)}_k - \dot{u}^{(3)}_k), \qquad (12) \\
\sigma^{(2)}_{,i} &= \rho^{12}_{ik}\ddot{u}^{(1)}_k + \rho^{22}_{ik}\ddot{u}^{(2)}_k + \rho^{23}_{ik}\ddot{u}^{(3)}_k \\
&\quad - b^{12}_{ik}(\dot{u}^{(1)}_k - \dot{u}^{(2)}_k) + b^{23}_{ik}(\dot{u}^{(2)}_k - \dot{u}^{(3)}_k), \qquad (13) \\
\sigma^{(3)}_{ij,j} &= \rho^{13}_{ik}\ddot{u}^{(1)}_k + \rho^{23}_{ik}\ddot{u}^{(2)}_k + \rho^{33}_{ik}\ddot{u}^{(3)}_k \\
&\quad - b^{13}_{ik}(\dot{u}^{(1)}_k - \dot{u}^{(3)}_k) - b^{23}_{ik}(\dot{u}^{(2)}_k - \dot{u}^{(3)}_k), \qquad (14)
\end{aligned}$$

where the diagonal $\rho^{\alpha\alpha}_{ik}$ are the effective inertias of the individual phases, the off-diagonal $\rho^{\alpha\beta}_{ik}$ $(\alpha \neq \beta)$ describe the inertial drag between phases, and b^{12}_{ik}, b^{13}_{ik}, and b^{23}_{ik} are the viscous friction tensors of the three contacting pairs. Both K and $\mathcal{R}$ coincide with their counterparts in the non-piezoelectric three-phase poroelastic theory [17,18,21]; the piezoelectric coupling enters the equations of motion only through W.

Variation with respect to the electric potential supplies the last field equation. Because W involves Φ only through $E_k = -\Phi_{,k}$ and neither K nor $\mathcal{R}$ contains $\dot{\Phi}$, the Φ-variation yields, in the absence of free volume charge, Gauss's law

$$D_{i,i} = 0. \tag{15}$$

The constitutive relations (5)–(8), the equations of motion (12)–(14), and Gauss's law (15) together constitute the governing equations of the three-phase porous piezoelectric medium. With D_i given by Eq. (8), Eq. (15) determines the electric potential Φ from the instantaneous skeleton strain and thereby closes the system. They describe body waves in an unbounded homogeneous medium, and their only electrical condition is Eq. (15), the quasi-static Gauss law in the absence of free volume charge. No electrode and no external circuit is imposed, so the formulation corresponds to the unbounded-medium case rather than to the short-circuit or open-circuit condition of a finite electroded sample.

2.2. Plane-wave solution and the Christoffel equation

We seek harmonic plane-wave solutions of the governing equations propagating along the unit vector n_k,

$$(u_j^{(1)}, u_j^{(2)}, u_j^{(3)}, \Phi) = (B_j, F_j, W_j, G)\, \exp\Big[\mathrm{i}\omega\Big(\frac{n_k x_k}{v} - t\Big)\Big], \tag{16}$$

where B_j, F_j, W_j, and G are the complex displacement and potential amplitudes, ω is the angular frequency, and v is the complex velocity. Under this substitution, $\partial_k \to \mathrm{i}\omega n_k/v$ and $\partial_t \to -\mathrm{i}\omega$, so that the inertial and frictional terms of Eqs. (12)–(14) combine into frequency-dependent effective complex densities

$$\begin{aligned}
\bar\rho_{ik}^{11} &= \rho_{ik}^{11} + \frac{\mathrm{i}}{\omega}(b_{ik}^{12} + b_{ik}^{13}), \quad \bar\rho_{ik}^{22} = \rho_{ik}^{22} + \frac{\mathrm{i}}{\omega}(b_{ik}^{12} + b_{ik}^{23}),\\
\bar\rho_{ik}^{33} &= \rho_{ik}^{33} + \frac{\mathrm{i}}{\omega}(b_{ik}^{13} + b_{ik}^{23}), \quad \bar\rho_{ik}^{12} = \rho_{ik}^{12} - \frac{\mathrm{i}}{\omega} b_{ik}^{12},\\
\bar\rho_{ik}^{13} &= \rho_{ik}^{13} - \frac{\mathrm{i}}{\omega} b_{ik}^{13}, \quad \bar\rho_{ik}^{23} = \rho_{ik}^{23} - \frac{\mathrm{i}}{\omega} b_{ik}^{23},
\end{aligned} \tag{17}$$

which carry the dissipation into the otherwise elastic dispersion relation.

At low frequencies the fluid-related friction coefficients are tied to the static permeability through the Darcy form: for the skeleton–pore-fluid pair, $b_0^{12} = \eta\phi_2^2/\kappa_0$ [6], with η the fluid viscosity, κ_0 the static permeability, and $\phi_2 = \phi(1 - S_3)$ the volume fraction of the pore fluid, where ϕ is the porosity and S_3 the filling-solid saturation of the pore space ($b_{ij}^{12} = \eta\phi_2^2[\kappa_{ij}]^{-1}$ for an anisotropic pore geometry [11]); the same form applies to the fluid–filling-solid pair b^{23}. The friction between the two solids arises instead from their grain-scale contact and is modelled by the empirical law $b^{13} = b_0^{13}[S_3\phi(1-\phi)]^2$ [20,21], with b_0^{13} a reference coefficient.

This constant, real-valued form is the low-frequency limit of the viscous drag. It is appropriate for $f \ll f_\mathrm{B}$, where the oscillatory pore flow keeps a fully developed (Poiseuille) profile, and the crossover to the inertia-dominated regime is set by the Biot characteristic frequency $f_\mathrm{B} = \eta\phi_2/(2\pi\alpha_\infty\rho^{(2)}\kappa_0)$, with $\rho^{(2)}$ the fluid density and $\alpha_\infty \geq 1$ the tortuosity of the fluid-filled pore space. Above the crossover the drag becomes frequency dependent in its own right: the static permeability is then replaced by a dynamic one, $b^{12}(\omega) = \eta\phi_2^2/\kappa^{12}(\omega)$ [36], whose complex value modifies the viscous loss and the added inertia together. The contact friction b^{13} arises from grain contact rather than viscous pore flow, so this correction does not apply to it. Subsection 3.1 locates the source band relative to f_B and states how the constant coefficients are used here. Through the imaginary parts of Eq. (17) the friction coefficients make the velocity v complex, and the resulting attenuation is examined in Subsection 3.6.

Substituting the plane-wave ansatz (16) into the governing equations gives a homogeneous linear

system for the amplitudes B_k, F_k, W_k, and G,

$$[c^{(11)}_{ijkl}n_jn_l - \bar{\rho}^{11}_{ik}v^2]B_k + [m^{(12)}_{ij}n_jn_k - \bar{\rho}^{12}_{ik}v^2]F_k + [c^{(13)}_{ijkl}n_jn_l - \bar{\rho}^{13}_{ik}v^2]W_k + e_{kij}n_kn_j\,G = 0, \tag{18}$$

$$[m^{(12)}_{kj}n_in_j - \bar{\rho}^{12}_{ik}v^2]B_k + [Rn_in_k - \bar{\rho}^{22}_{ik}v^2]F_k + [m^{(32)}_{kj}n_in_j - \bar{\rho}^{23}_{ik}v^2]W_k = 0, \tag{19}$$

$$[c^{(13)}_{ijkl}n_jn_l - \bar{\rho}^{13}_{ik}v^2]B_k + [m^{(32)}_{ij}n_jn_k - \bar{\rho}^{23}_{ik}v^2]F_k + [c^{(33)}_{ijkl}n_jn_l - \bar{\rho}^{33}_{ik}v^2]W_k = 0, \tag{20}$$

$$e_{ikl}n_in_l\,B_k - \xi_{ij}n_in_j\,G = 0. \tag{21}$$

Equations (18)–(21) constitute the Christoffel equation of the three-phase porous piezoelectric medium. Collecting the ten unknowns into $\boldsymbol{U} = (B_1, B_2, B_3, F_1, F_2, F_3, W_1, W_2, W_3, G)^{\mathrm{T}}$, they take the matrix form $\boldsymbol{M}(v, \boldsymbol{n})\,\boldsymbol{U} = \boldsymbol{0}$, whose nontrivial solutions require

$$\det \boldsymbol{M}(v, \boldsymbol{n}) = 0. \tag{22}$$

For each propagation direction, Eq. (22) is a polynomial in v^2 whose complex roots give the bulk modes of the medium. For a plane wave, Gauss's law (15) reduces to $n_iD_i = 0$, the statement carried by Eq. (21): the electric displacement stays perpendicular to the propagation direction.

Because the medium is transversely isotropic about the poling axis z, any plane containing that axis is representative for plane-wave analysis, and we adopt the sagittal plane $n_2 = 0$. Writing the propagation direction as $n_1 = \sin\theta$, $n_2 = 0$, $n_3 = \cos\theta$, with θ measured from the poling axis, the 10×10 system separates into two independent subsystems, a 7×7 in-plane block involving $(B_1, B_3, F_1, F_3, W_1, W_3, G)$ and a 3×3 antiplane block involving (B_2, F_2, W_2), which support two distinct families of body waves. Their explicit nonzero entries are given in Appendix A. The antiplane block contains neither the piezoelectric constants e_{kij} nor the dielectric constants ξ_{ij}, and the reason is physical. The antiplane skeleton motion carries only the shear strains $\varepsilon^{(1)}_{12}$ and $\varepsilon^{(1)}_{23}$; for the 6mm tensor, $\varepsilon^{(1)}_{12}$ induces no electric displacement, while $\varepsilon^{(1)}_{23}$ induces, through e_{15}, only the electric-displacement component perpendicular to the sagittal plane. The fields of a plane wave with $n_2 = 0$ are uniform along that direction, so this component contributes nothing to $D_{i,i}$ and drops out of Gauss's law (15): the SH motion generates no electric field and receives no piezoelectric stiffening. Conversely, an electric field in the sagittal plane produces, through e_{15}, e_{31}, and e_{33}, only stresses acting on the in-plane motion, none on the SH polarization. Both piezoelectric channels therefore vanish, and no choice of the piezoelectric constants affects the SH waves in this plane. The pore fluid and the filling solid, being non-piezoelectric, add no further coupling, so the antiplane motion of all three phases is decoupled from the electric field, generalizing the corresponding two-phase result [13] to three phases. The phase and group velocities of the two families are analysed in Section 3.

Each complex root v of Eq. (22) determines a phase velocity and an attenuation coefficient,

$$v_{\mathrm{p}} = [\mathrm{Re}(1/v)]^{-1}, \qquad \alpha = \omega\,\mathrm{Im}(1/v). \tag{23}$$

With θ defined as above, the magnitude and direction ψ of the group velocity follow from the phase-velocity surface as

$$|\boldsymbol{v}_{\mathrm{g}}| = \sqrt{v_{\mathrm{p}}^2 + \left(\frac{\partial v_{\mathrm{p}}}{\partial\theta}\right)^2}, \qquad \psi = \theta + \arctan\left(\frac{1}{v_{\mathrm{p}}}\frac{\partial v_{\mathrm{p}}}{\partial\theta}\right), \tag{24}$$

equivalently obtained by applying the implicit-function theorem to Eq. (22). Equations (23) and (24) yield the phase velocity, group velocity, and attenuation of every mode as functions of propagation direction, and serve as the analytical reference for the simulations that follow.

Equation (24) is constructed from the angular derivative of a real phase-velocity surface and is used here only for the frictionless reference state of all velocity results below. In that state the effective densities of Eq. (17) reduce to the real $\rho_{ik}^{\alpha\beta}$, the Christoffel system carries no frequency, and α vanishes, so the medium is conservative and non-dispersive and Eq. (24) gives the exact group velocity $\boldsymbol{v}_{\mathrm{g}} = \nabla_{\boldsymbol{k}}\omega$. Interphase friction changes this: $\bar{\rho}_{ik}^{\alpha\beta}(\omega)$ makes v complex and frequency dependent, and a strict group velocity then requires the frequency derivative $\partial\bar{\rho}_{ik}^{\alpha\beta}/\partial\omega$ of the dispersion relation as well. Subsection 3.6 therefore characterizes the dissipative modes by the attenuation coefficient α and the inverse quality factor formed from the same complex root, not by Eq. (24). The group velocity is also distinct from the energy velocity, the ratio of the time-averaged energy flux to the time-averaged energy density: the two coincide for conservative anisotropic media [10] but are not identified with each other where dissipation is present.

2.3. Staggered-grid finite-difference scheme

For time-domain wavefield simulation, we discretize the governing equations on a two-dimensional staggered grid in the x–z sagittal plane, where z is the poling axis of the transversely isotropic skeleton. This two-dimensional formulation captures the five in-plane modes and the coupled electric-potential response; the two antiplane SH modes lie outside it and are analysed only through the Christoffel subsystem of Subsection 2.2. Eighth-order central differences are used in space and a leapfrog scheme in time. The fields follow the standard velocity–stress layout shown in Fig. 1: the normal stresses $\sigma_{xx}^{(1)}, \sigma_{zz}^{(1)}, \sigma^{(2)}, \sigma_{xx}^{(3)}, \sigma_{zz}^{(3)}$ are stored at the integer node (i, j), the shear stresses $\sigma_{xz}^{(1)}, \sigma_{xz}^{(3)}$ at $(i+\frac{1}{2}, j+\frac{1}{2})$, the horizontal velocities $v_x^{(\alpha)}$ at $(i+\frac{1}{2}, j)$, and the vertical velocities $v_z^{(\alpha)}$ together with the electric-potential rate $\dot{\Phi}$ at $(i, j+\frac{1}{2})$.

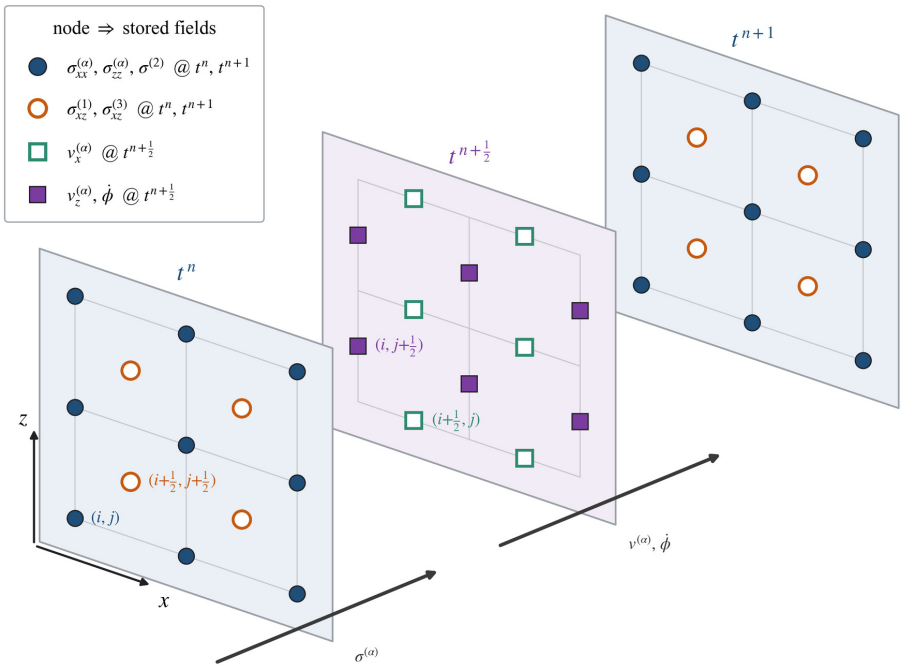


Fig. 1. (color online) Staggered-grid layout of the field variables for the coupled electromechanical poroelastic scheme in the x–z plane (z is the poling axis).

Each time step is advanced in three stages.

In the first stage the velocities are updated from the stresses at level n. With D_x and D_z the staggered difference operators, the effective driving term $\Pi_{\beta x}$ of phase β in the x direction combines the stress gradient with the interphase friction,

$$\begin{aligned}
\Pi_{1x} &= D_x\sigma^{(1)}_{xx} + D_z\sigma^{(1)}_{xz} - b^{12}_{xx}(v^{(1)}_x - v^{(2)}_x) - b^{13}_{xx}(v^{(1)}_x - v^{(3)}_x),\\
\Pi_{2x} &= D_x\sigma^{(2)} + b^{12}_{xx}(v^{(1)}_x - v^{(2)}_x) - b^{23}_{xx}(v^{(2)}_x - v^{(3)}_x),\\
\Pi_{3x} &= D_x\sigma^{(3)}_{xx} + D_z\sigma^{(3)}_{xz} + b^{13}_{xx}(v^{(1)}_x - v^{(3)}_x) + b^{23}_{xx}(v^{(2)}_x - v^{(3)}_x),
\end{aligned} \tag{25}$$

where $b^{\alpha\beta}_{xx}$ are the friction coefficients along x. Evaluating $\Pi_{\beta x}$ at level n and node $(i{+}1/2, j)$, the horizontal velocities advance as

$$v^{(\alpha)(n+1/2)}_{x(i+1/2,j)} = v^{(\alpha)(n-1/2)}_{x(i+1/2,j)} + \Delta t \sum_{\beta=1}^{3} \gamma_{\alpha\beta}\, \Pi^{(n)}_{\beta x\,(i+1/2,j)}, \quad \alpha = 1,2,3, \tag{26}$$

where $\gamma_{\alpha\beta}$ are the entries of the inverse of the 3×3 density matrix $[\rho^{\alpha\beta}]$, and the friction terms in $\Pi_{\beta x}$ are taken explicitly at the previous half step. The vertical velocities $v^{(\alpha)}_z$ at $(i, j+1/2)$ are updated in the same way.

In the second stage the electric-potential rate is obtained from the just-updated skeleton velocities. Because only phase 1 is piezoelectric, differentiating Gauss's law (15) in time and using Eq. (8) yields a Poisson equation for $\dot\Phi$,

$$\begin{aligned}
\xi_{11}D_x^2\dot\Phi^{(n+1/2)}_{(i,j+1/2)} + \xi_{33}D_z^2\dot\Phi^{(n+1/2)}_{(i,j+1/2)} &= D_x\big[e_{15}(D_z v^{(1)}_x + D_x v^{(1)}_z)\big]^{(n+1/2)}_{(i,j+1/2)}\\
&\quad + D_z\big[e_{31}D_x v^{(1)}_x + e_{33}D_z v^{(1)}_z\big]^{(n+1/2)}_{(i,j+1/2)},
\end{aligned} \tag{27}$$

which is solved on the grid at every time step. Retaining this coupling—rather than setting $\partial D_i/\partial t = 0$, which would slave the electric field to the instantaneous strain—avoids the artificial stiffening noted in Section 1.

In the third stage the stresses are advanced to level $n+1$ using the updated velocities and $\dot\Phi$. In Voigt notation, the skeleton stresses update as

$$\begin{aligned}
\sigma^{(1)(n+1)}_{xx(i,j)} &= \sigma^{(1)(n)}_{xx(i,j)} + \Delta t\big[\, c^{(11)}_{11}D_x v^{(1)}_x + c^{(11)}_{13}D_z v^{(1)}_z + m^{(12)}_{11}(D_x v^{(2)}_x + D_z v^{(2)}_z)\\
&\quad + c^{(13)}_{11}D_x v^{(3)}_x + c^{(13)}_{13}D_z v^{(3)}_z + e_{31}D_z\dot\Phi\,\big]^{(n+1/2)}_{(i,j)},
\end{aligned} \tag{28}$$

$$\begin{aligned}
\sigma^{(1)(n+1)}_{zz(i,j)} &= \sigma^{(1)(n)}_{zz(i,j)} + \Delta t\big[\, c^{(11)}_{13}D_x v^{(1)}_x + c^{(11)}_{33}D_z v^{(1)}_z + m^{(12)}_{33}(D_x v^{(2)}_x + D_z v^{(2)}_z)\\
&\quad + c^{(13)}_{13}D_x v^{(3)}_x + c^{(13)}_{33}D_z v^{(3)}_z + e_{33}D_z\dot\Phi\,\big]^{(n+1/2)}_{(i,j)},
\end{aligned} \tag{29}$$

$$\begin{aligned}
\sigma^{(1)(n+1)}_{xz(i+1/2,j+1/2)} &= \sigma^{(1)(n)}_{xz(i+1/2,j+1/2)} + \Delta t\big[\, c^{(11)}_{44}(D_z v^{(1)}_x + D_x v^{(1)}_z)\\
&\quad + c^{(13)}_{44}(D_z v^{(3)}_x + D_x v^{(3)}_z) + e_{15}D_x\dot\Phi\,\big]^{(n+1/2)}_{(i+1/2,j+1/2)}.
\end{aligned} \tag{30}$$

The pore-fluid stress $\sigma^{(2)}$ at (i,j) and the filling-solid stresses (for the isotropic phase 3, $c^{(33)}_{11} = c^{(33)}_{33} = \lambda_3 + 2\mu_3$, $c^{(33)}_{13} = \lambda_3$, $c^{(33)}_{44} = \mu_3$) are advanced in the same manner from the constitutive relations (6)

and (7), but contain no piezoelectric term; the electromechanical coupling thus enters only through the $\dot{\Phi}$ terms of Eqs. (28)–(30). The open domain is truncated by the absorbing layer of Subsection 2.4.

Two time-step restrictions apply to the explicit scheme. The first is the Courant–Friedrichs–Lewy (CFL) condition of the eighth-order staggered operator. A von Neumann analysis of the velocity–stress update gives, for the square grid used here,

$$\Delta t \le \frac{h}{\sqrt{2}\, S\, v_{\max}}, \qquad S = \sum_{m=1}^{4} |a_m|, \tag{31}$$

where $h = \Delta x = \Delta z$, the a_m are the coefficients of the eighth-order staggered difference operator, and $v_{\max}$ is the largest phase velocity supported by the coupled medium. Because the piezoelectric coupling stiffens the skeleton, $v_{\max}$ must be taken from the stiffened Christoffel solution rather than from a single-phase estimate. The electric potential follows from an elliptic solve at every step and carries no wave speed of its own, so it adds no separate restriction; the electromechanical coupling enters the stability limit only through the stiffened $v_{\max}$.

The second restriction comes from the interphase friction, which is integrated explicitly. Retaining only the friction terms of Eqs. (12)–(14) leaves the relaxation system $\dot{\boldsymbol{v}} = -\boldsymbol{\rho}^{-1}\boldsymbol{B}\boldsymbol{v}$, in which $\boldsymbol{v}$ collects the three phase velocities along one coordinate, $\boldsymbol{\rho} = [\rho_{ik}^{\alpha\beta}]$ is the density matrix, and

$$\boldsymbol{B} = \begin{pmatrix} b^{12} + b^{13} & -b^{12} & -b^{13} \\ -b^{12} & b^{12} + b^{23} & -b^{23} \\ -b^{13} & -b^{23} & b^{13} + b^{23} \end{pmatrix}. \tag{32}$$

Advancing this system explicitly is stable for

$$\Delta t \le \frac{2}{\lambda_{\max}}, \qquad \boldsymbol{B}\boldsymbol{q} = \lambda\, \boldsymbol{\rho}\, \boldsymbol{q}, \tag{33}$$

where the generalized eigenvalues λ are real and non-negative. One of them vanishes: in-phase motion of the three phases involves no relative velocity and is not damped. The two bounds constrain different mechanisms and are therefore quoted separately; neither is claimed to be sufficient for the fully coupled update. Their values for the medium considered below, together with convergence tests of the scheme, are given in Appendix C.

2.4. Coupled electromechanical perfectly matched layer

Because the computational grid is finite, the domain is truncated by a perfectly matched layer that absorbs outgoing waves with low spurious reflection. Here the absorber is nontrivial: it must damp both the coupled motion of the three phases and the electromechanical coupling carried by the skeleton, which is tied at every step to the potential rate $\dot{\Phi}$ through the Poisson solve of Eq. (27). A mechanical-only layer that clamped $\dot{\Phi}$ at the inner edge would make this coupling discontinuous and reflect part of the wavefield. We therefore use a *coupled electromechanical* PML, in which split-field damping acts on the velocities and stresses of all three phases while $\dot{\Phi}$ is solved consistently throughout the absorbing region.

The main domain is bordered by N_{PML} layers, damped along x in the side strips, along z in the top and bottom strips, and along both directions in the corners.

Following the split-field formulation for poroelastic and anisotropic media [25,29,30], the absorption is set by two damping profiles growing quadratically from the inner edge,

$$d_x(x) = \frac{3v_{\mathrm{P}}}{2L_x} \ln\frac{1}{R_0} \left(\frac{x}{L_x}\right)^2, \qquad d_z(z) = \frac{3v_{\mathrm{P}}}{2L_z} \ln\frac{1}{R_0} \left(\frac{z}{L_z}\right)^2, \tag{34}$$

where $L_x = N_{\mathrm{PML}}\Delta x$ and $L_z = N_{\mathrm{PML}}\Delta z$ are the layer thicknesses, v_{P} a reference fast-wave speed, R_0 the target reflection coefficient, and the local coordinates x, z are measured inward from the inner edge; d_x and d_z are damping functions, distinct from the difference operators D_x, D_z.

Inside the layer each mechanical component is split into an x-part and a z-part, for example $v_x^{(\alpha)} = v_x^{(\alpha),x} + v_x^{(\alpha),z}$, each advanced from its own derivative and damped by the corresponding profile. Writing $\mathcal{S}_x$ for the part of the interior right-hand side of Eqs. (26) and (28)–(30) that carries the x-derivatives, together with the friction terms of the velocity updates, the x-part of a generic component q advances as

$$q^{x,\,n+1} = \frac{1/\Delta t - d_x/2}{1/\Delta t + d_x/2}\, q^{x,\,n} + \frac{1}{1/\Delta t + d_x/2}\, \mathcal{S}_x^{n+1/2}, \tag{35}$$

the z-part following in the same way with d_z and $\mathcal{S}_z$, and the total field recovered as $q = q^x + q^z$. For $d_x = d_z = 0$ this reduces to the interior update, so the scheme of Subsection 2.3 is recovered continuously across the inner edge.

The potential rate is treated differently because it is quasi-static: $\dot\Phi$ is recovered instantaneously from the elliptic solve of Eq. (27) rather than time-marched, so there is no split field to damp. Instead, Eq. (27) is assembled over the *entire* grid—main domain and PML layers together—with a homogeneous condition on the outer frame. The piezoelectric source then follows the attenuating velocities into the layer, and the resulting $\dot\Phi$ re-enters the stress updates through the $e_{31}D_z\dot\Phi$, $e_{33}D_z\dot\Phi$, and $e_{15}D_x\dot\Phi$ terms of Eqs. (28)–(30). Mechanical absorption and the electric solve thus stay coupled throughout the layer, so the skeleton, pore fluid, filling solid, and electric field decay together rather than the electric field being truncated at the main-domain boundary.

Figure 2 uses the electric response itself as a diagnostic, showing the final-time $\dot\Phi$ in the main domain under the three boundary treatments. Without an absorber [Fig. 2(a)], the outgoing fronts have reached the edges and returned, overlaying the interior with edge and corner reflections. A mechanical-only PML [Fig. 2(b)] removes most of the elastic reflection but leaves residual $\dot\Phi$ near the boundaries, where the clamped potential rate is inconsistent with the decaying motion. The coupled electromechanical PML [Fig. 2(c)] suppresses both, leaving the interior dominated by the physical outgoing fronts. The coupled absorber is thus required not for the mechanical fields alone but also for the electric response driven by them.

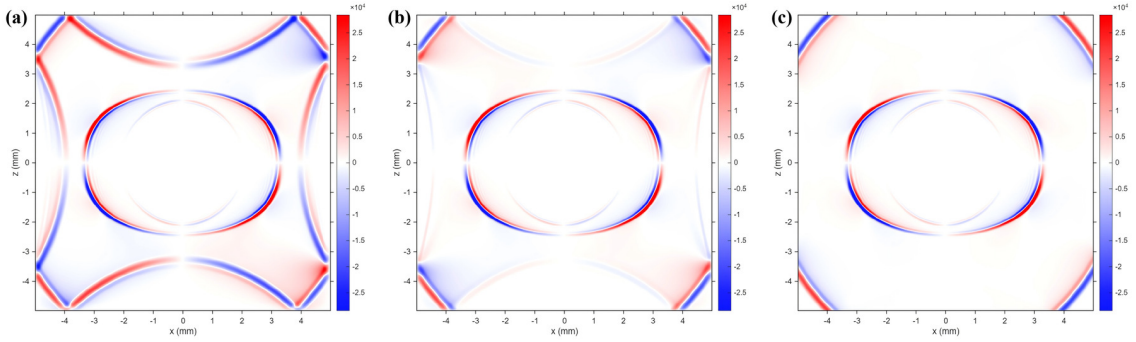


Fig. 2. (color online) Snapshot of the electric-potential rate $\dot{\Phi}$ in the main domain, showing its reflection under three boundary treatments: (a) no PML, (b) mechanical-only PML, and (c) coupled electromechanical PML.

The residual reflection is quantified by comparing each truncated-domain computation with a reference computation on an enlarged grid without the absorbing layer, following established practice for assessing a perfectly matched layer [37,38]. The reference domain is large enough that no mechanical return from its outer boundary reaches the receivers within the analysis window. Writing $\boldsymbol{v}_{\mathrm{PML}}$ and $\boldsymbol{v}_{\mathrm{ref}}$ for the skeleton velocity recorded at a given receiver in the two computations, the numerical reflection coefficient is evaluated as the maximum relative reflection error

$$R(\theta) = \frac{\max_{t\in W} \|\boldsymbol{v}_{\mathrm{PML}}(t,\theta) - \boldsymbol{v}_{\mathrm{ref}}(t,\theta)\|}{\max_{t\in W} \|\boldsymbol{v}_{\mathrm{ref}}(t,\theta)\|}, \qquad R_{\mathrm{dB}}(\theta) = 20\log_{10} R(\theta), \tag{36}$$

where the two velocity components are subtracted before the vector norm is taken, W is the analysis window, and the incidence angle θ is measured with respect to the boundary normal. Appendix D reports R_{dB} over a range of nominal source frequencies, incidence angles, and layer thicknesses. For $N_{\mathrm{PML}} = 80$, R_{dB} stays below about -32 dB from 1.5 to 4.5 MHz and from 0° to 45°, and reaches -42.0 dB at 3.0 MHz and normal incidence.

3. Numerical results and discussion

We now apply the analytical Christoffel solution and the staggered-grid FDTD scheme to a representative three-phase porous piezoelectric medium. Subsection 3.1 specifies the material parameters and the numerical setup shared by the two methods. Subsection 3.2 reports the analytical phase and group velocities, which provide the reference for the simulations. Subsection 3.3 presents the simulated wavefields and verifies their arrival times against this reference. Subsection 3.4 benchmarks the scheme in reduced limits, against an independent finite-element solution and against published results. Subsection 3.5 isolates the effect of the piezoelectric coupling on the wave modes, and Subsection 3.6 examines how the interphase friction coefficients govern the attenuation of the slow waves.

3.1. Material parameters and numerical setup

The medium used throughout this section consists of a transversely isotropic PZT-2 skeleton, a representative water-like pore fluid, and an isotropic filling solid (hereafter the infill) representative of a polymer, with only the skeleton being piezoelectric. Table 1 lists the constituent and skeleton parameters of

the three phases together with the porosity ϕ and the filling-solid saturation S_3. Here A_{IJ} (Voigt notation) denote the drained-frame stiffness constants of the porous skeleton. The pore fluid is representative rather than material specific: the value $K_{\mathrm{f}} = 3.5$ GPa is adopted as an effective parameter of the model and is not intended to reproduce the tabulated bulk modulus of pure water. The parameter set is chosen to expose the wave modes and the coupling mechanisms of a three-phase porous piezoelectric medium rather than to characterize one particular material. The coefficients that enter the governing equations are set in three ways. The stiffness tensors $c^{(11)}_{ijkl}$, $c^{(13)}_{ijkl}$, $c^{(33)}_{ijkl}$, the fluid modulus R, and the solid–fluid couplings $m^{(12)}_{ij}$, $m^{(32)}_{ij}$ are not assigned independently: they are constructed using the entries of Table 1, the closed-form three-phase relations of poroelasticity [17,18], and the closure relations stated in Appendix B, which also records how the skeleton parameter set is obtained and reports a positive-definiteness check of the assembled stiffness matrix. The density matrix $\rho^{\alpha\beta}_{ik}$ is a representative effective set, listed in full in Appendix B, which returns the phase masses and is positive definite; its closure calls for interface-geometry parameters that the constituent data of Table 1 do not by themselves fix, and we do not identify these from a particular pore geometry. The friction coefficients $b^{\alpha\beta}_{ik}$ are prescribed separately, as specified below. For the representative numerical model considered here, the inertia and friction tensors are taken to be spatially isotropic, $\rho^{\alpha\beta}_{ik} = \rho^{\alpha\beta}\delta_{ik}$ and $b^{\alpha\beta}_{ik} = b^{\alpha\beta}\delta_{ik}$.

Table 1. Constituent and skeleton parameters of the representative three-phase medium.

Phase	Parameter	Value
Skeleton (PZT-2, 6mm)	density $\rho^{(1)}$	7600 kg/m^3
	drained frame A_{11}, A_{12}, A_{13}	46.4, 14.2, 12.4 (GPa)
	drained frame A_{33}, A_{44}, A_{66}	38.5, 12.5, 16.1 (GPa)
	grain bulk modulus $K_{\mathrm{s}1}$	96.9 GPa
	piezoelectric e_{15}, e_{31}, e_{33}	2.67, -0.12, 4.15 (C/m^2)
	clamped permittivity ξ_{11}, ξ_{33}	2.58, 1.13 ($\times 10^{-9}$ F/m)
Pore fluid (representative)	density $\rho^{(2)}$	1000 kg/m^3
	bulk modulus K_{f}	3.5 GPa
	viscosity η	1.0×10^{-3} Pa·s
Filling solid	density $\rho^{(3)}$	1200 kg/m^3
	grain bulk, shear modulus $K_{\mathrm{s}3}, \mu_{\mathrm{s}3}$	9.0, 1.5 (GPa)
Geometry	porosity ϕ	0.4
	saturation S_3	0.7
	static permeability κ_0	1×10^{-13} m^2
	percolation exponent n	3.8

The same material set drives the Christoffel analysis and the FDTD simulation. Throughout Subsections 3.2–3.5 the interphase friction is switched off, $b^{12} = b^{13} = b^{23} = 0$, so that the phase and group velocities, the arrival times, and the comparison with and without the piezoelectric coupling all refer to one conservative reference state; nonzero friction is introduced only in the attenuation study of Subsection 3.6, where b^{12} and b^{13} are swept over several decades. The swept values are independent coefficients, not Darcy values tied to the permeability of Table 1. For the parameters of Table 1, the characteristic frequency of Subsection 2.2 has the conservative upper estimate $f_{\mathrm{B}} \le \eta\phi_2/(2\pi\rho^{(2)}\kappa_0) = 0.19$ MHz, since $\alpha_\infty \ge 1$; the 3 MHz centre frequency of the source therefore lies on its high-frequency side by more than a factor of 15. Predicting the fluid-related attenuation of a specific material in this band would accordingly

call for a dynamic-permeability correction. The results reported below do not rest on such a prediction: Subsections 3.2–3.5 carry no friction at all, and Subsection 3.6 varies the coefficients independently at a single centre frequency, so that the frequency dependence of the drag on any one material is not at issue. The FDTD domain is an 800×800 grid with $\Delta x = \Delta z = 12.5\ \mu$m, corresponding to a physical size of $10 \times 10\ \mathrm{mm}^2$, surrounded on every side by $N_{\mathrm{PML}} = 80$ absorbing layers, and is advanced with a time step $\Delta t = 0.1$ ns using eighth-order spatial differences. For the present parameters, Eq. (31) gives the CFL limit $\Delta t_{\mathrm{CFL}} = 1.93$ ns, so this step is about 19 times smaller and satisfies the CFL requirement; see Appendix C for the friction-related stability bound and convergence tests. The field is excited at the centre of the domain by a Ricker point source applied to the skeleton vertical velocity, with peak frequency $f_{\mathrm{p}} = 3$ MHz and causal delay $t_0 = 1.2/f_{\mathrm{p}} = 0.4\ \mu$s; this peak frequency keeps the slow modes, whose wavelengths are of the order of 0.2 mm, well resolved by the grid. A circular array of 72 receivers at radius $r_0 = 3.0$ mm, spaced 5° apart, records the wavefield for the arrival-time analysis.

3.2. Analytical phase and group velocities

Applying the Christoffel procedure of Subsection 2.2 to the anisotropic two-solid, one-fluid medium yields the velocities shown in Fig. 3. Each propagation direction supports seven body-wave modes: three quasi-compressional waves (qP1, qP2, qP3), two quasi-shear waves (qSV1, qSV2), and two horizontally polarized shear waves (SH1, SH2). This count reflects the symmetry of the skeleton. An isotropic, non-piezoelectric three-phase medium of the Leclaire–Carcione type carries only five waves—three compressional and two shear—because the two shear polarizations are degenerate within each solid [17,18]. The transverse isotropy of the piezoelectric skeleton lifts this degeneracy, splitting each shear wave into an in-plane quasi-shear branch and an out-of-plane SH branch and thereby raising the count to seven. The separation matches the decomposition of Subsection 2.2, in which the 7×7 in-plane block yields qP1, qP2, qP3, qSV1, and qSV2 and the 3×3 antiplane block yields SH1 and SH2. Figure 3(a) and 3(b) show the phase-velocity and group-velocity polar diagrams of these modes, computed from the roots of Eq. (22) over all propagation directions. Because the interphase friction coefficients vanish in this conservative reference state, the velocities shown in Fig. 3 are independent of frequency.

Among the seven modes, each is borne predominantly by one constituent of the medium. The waves qP1 and qSV1 are the fast compressional and shear waves of the piezoelectric skeleton; qP2 and qSV2 are the compressional and shear waves of the filling solid; and qP3 is the fluid-borne Biot slow wave. This assignment follows from the dominant stiffness and inertia that each branch samples. The piezoelectric coupling, carried by the skeleton, further modulates the in-plane modes.

Away from the poling axis every branch becomes direction-dependent, reflecting the 6mm symmetry of the skeleton. Figure 3(c) shows the polarization angle of the five in-plane modes, defined so that 0° marks a purely compressional and 90° a purely shear particle motion; this angle distinguishes the quasi-compressional from the quasi-shear branches and so provides the basis for the mode assignment above. The two SH waves are obtained separately, from the decoupled 3×3 antiplane subsystem, and are polarized

perpendicular to the sagittal plane, so that their motion is purely shear. Because that subsystem contains no piezoelectric or dielectric constant, the SH waves are not modulated by the piezoelectric coupling, which extends the two-phase decoupling result of Vashishth and Gupta [13] to the multiphase porous piezoelectric medium.

The analytical phase and group velocities obtained from the Christoffel solution serve as the theoretical reference for the arrival times computed in the simulations that follow.

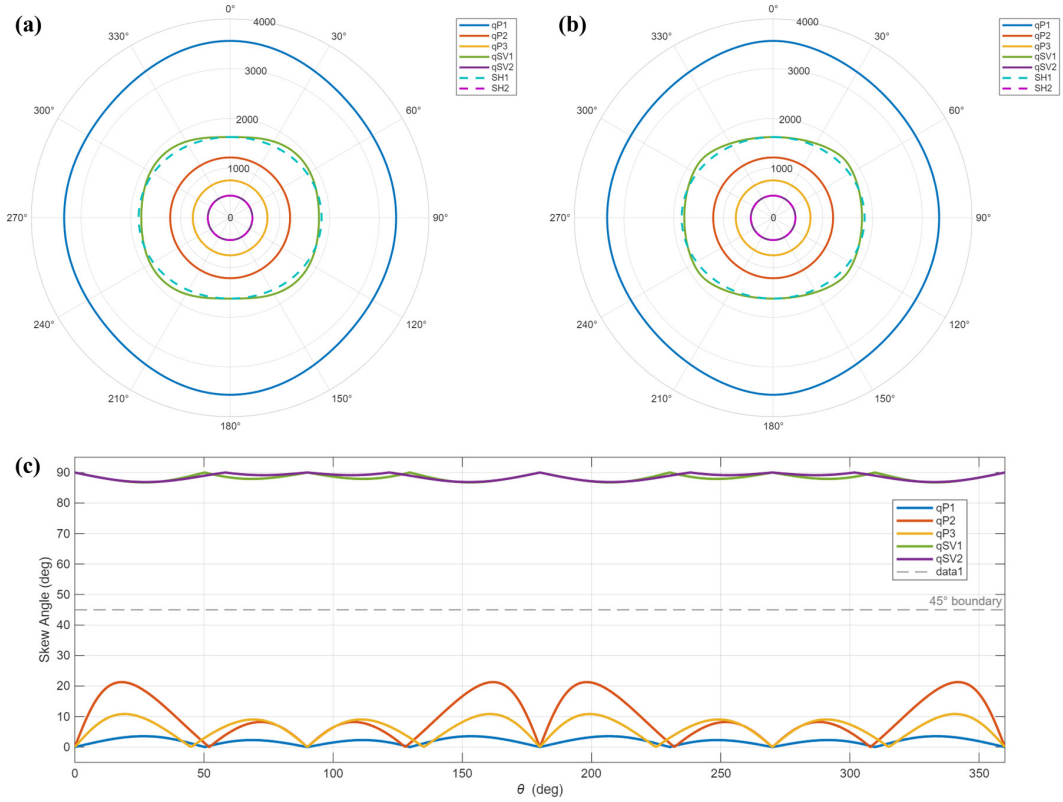


Fig. 3. (color online) Analytical velocities of the three-phase porous piezoelectric medium in the frictionless reference state, in which the velocities are frequency independent: (a) phase-velocity polar plot, (b) group-velocity polar plot, and (c) polarization angle of the five in-plane modes versus propagation angle.

3.3. Simulated wavefields and arrival-time verification

Following the FDTD scheme of Subsection 2.3, we simulate the two-dimensional wave propagation in the two-solid, one-fluid porous piezoelectric medium. Figure 4 shows a snapshot of the coupled wavefield at $t = 1.5\ \mu$s, displaying the skeleton velocities $v_x^{(1)}$ and $v_z^{(1)}$, the electric-potential rate $\dot{\Phi}$, the filling-solid velocity $v_z^{(3)}$, the pore-fluid velocity $v_z^{(2)}$, and the skeleton normal stress $\sigma_{zz}^{(1)}$. The mechanical fields form concentric wavefronts of different radii: the outermost front is the fast skeleton wave qP1, and the inner fronts are the slower filling-solid and fluid-borne modes, their radial separation reproducing the velocity ordering of Fig. 3. The fronts are slightly non-circular, the imprint of the skeleton anisotropy on the wavefield. Because the simulation is two-dimensional and confined to the sagittal plane, it does not capture the SH waves, whose motion is polarized perpendicular to that plane.

The electric-potential-rate panel shares the same fronts as the skeleton velocities rather than forming an independent pattern. Here $\dot{\Phi}$ is not a propagating wave of its own but an electric response generated by the skeleton motion through the Poisson equation (27); it simply accompanies the stress wave as that wave

passes. The filling-solid velocity shows the inner slow fronts clearly, whereas the pore-fluid velocity is more diffuse and lacks the sharp concentric fronts of the solid phases, consistent with the fluid participating mainly through its dilatational coupling to the two solids.

Figure 5 shows the full-angle B-scan recorded by the 72-receiver array for the skeleton velocity $v_z^{(1)}$, the skeleton stresses $\sigma_{zz}^{(1)}$ and $\sigma_{xz}^{(1)}$, the pore-fluid velocity $v_z^{(2)}$, the filling-solid velocity $v_z^{(3)}$, and the electric-potential rate $\dot{\Phi}$. In every field the arrivals form distinct bands whose bending across receiver angle reflects the anisotropy of the group velocity. The $\dot{\Phi}$ gather mirrors the skeleton-velocity gather, once more showing the electric response driven by the skeleton motion. Overlaying the theoretical peak-arrival times $t = r_0/|\boldsymbol{v}_{\mathrm{g}}(\theta)| + t_0$ obtained from the group velocities of Fig. 3(b), the simulated bands follow the analytical curves across all propagation directions; the maximum arrival-time discrepancy over the recorded modes and angles is below 15 ns, within 1% of the corresponding arrival times and well within the Ricker half-width. Refining either the grid spacing or the time step changes the simulated arrivals by no more than 0.13 ns, so this comparison is not limited by the discretization (Appendix C). The gather is free of reflections from the truncation boundary, confirming the effectiveness of the coupled electromechanical PML of Subsection 2.4.

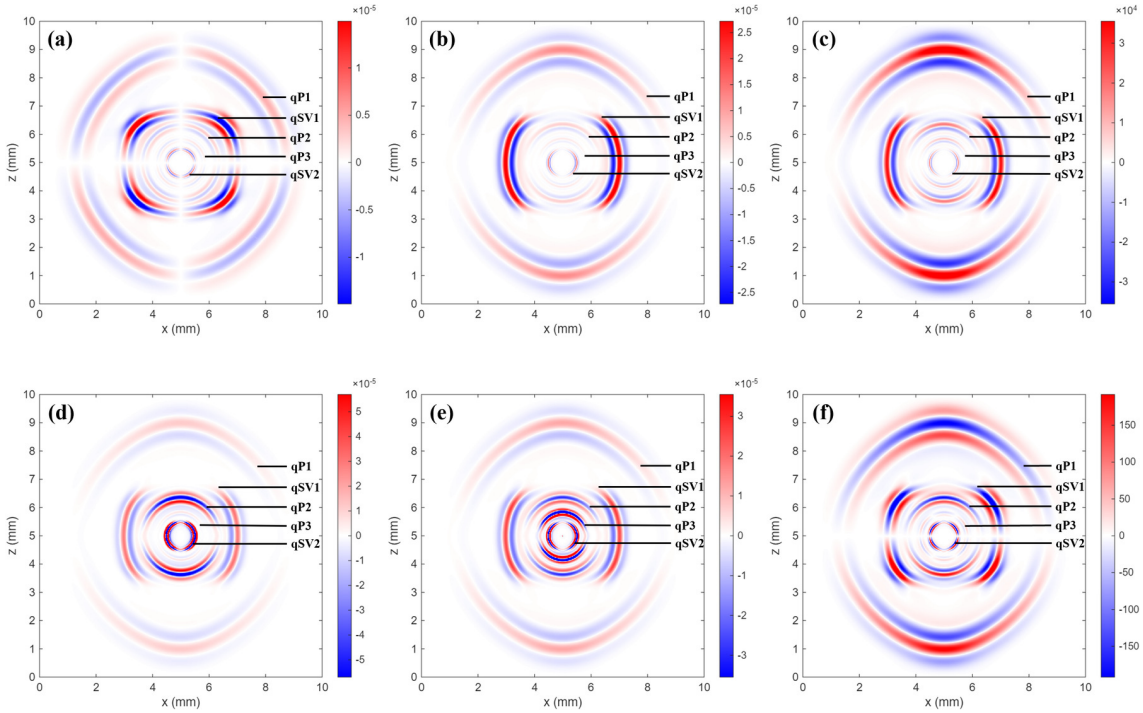


Fig. 4. (color online) Snapshot of the coupled wavefield at $t = 1.5$ μs: (a) skeleton velocity $v_x^{(1)}$, (b) skeleton velocity $v_z^{(1)}$, (c) electric-potential rate $\dot{\Phi}$, (d) filling-solid velocity $v_z^{(3)}$, (e) pore-fluid velocity $v_z^{(2)}$, and (f) skeleton normal stress $\sigma_{zz}^{(1)}$.

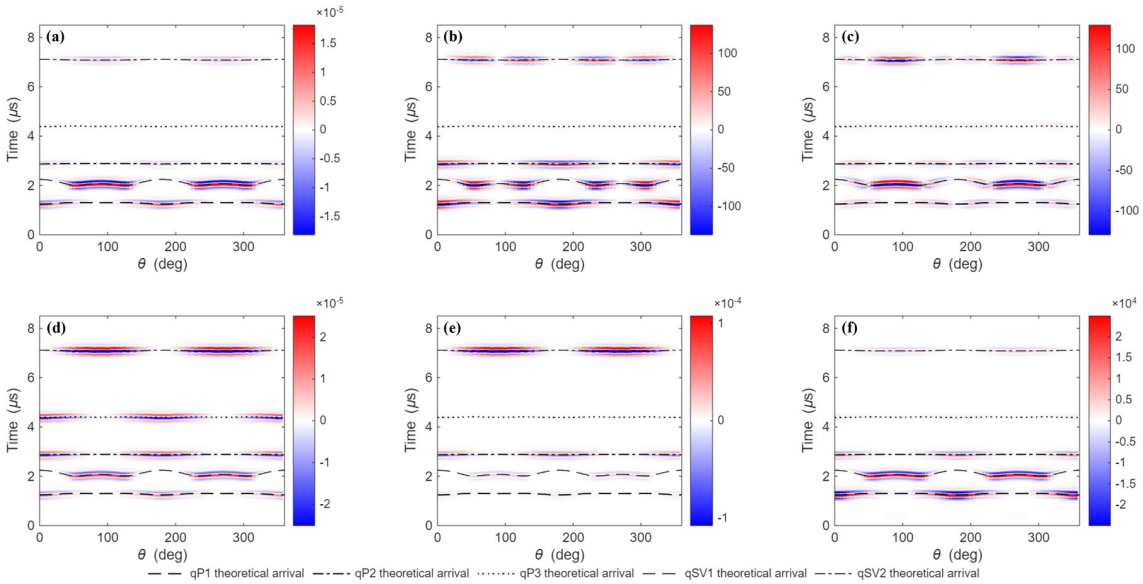


Fig. 5. (color online) Full-angle B-scan over the 72-receiver circular array ($r_0 = 3.0$ mm): (a) skeleton velocity $v_z^{(1)}$, (b) skeleton normal stress $\sigma_{zz}^{(1)}$, (c) skeleton shear stress $\sigma_{xz}^{(1)}$, (d) pore-fluid velocity $v_z^{(2)}$, (e) filling-solid velocity $v_z^{(3)}$, and (f) electric-potential rate $\dot{\Phi}$.

3.4. Benchmarks in reduced limits

To validate the time-domain scheme against an independent solver, we compare it with COMSOL in a reduced limit. The built-in COMSOL Poroelastic Waves interface is restricted to a non-piezoelectric, single-solid, single-fluid medium and to frequency-domain computation. We therefore reduce the present time-domain model to the same non-piezoelectric two-phase (single-solid, single-fluid) Biot medium, removing the filling solid and setting $e_{kij} = 0$. The COMSOL response is obtained by a frequency sweep followed by an inverse Fourier transform into the time domain, and the two time-domain results are then compared, with the Christoffel solution providing the analytical arrival reference. The reduced medium is a $\phi = 0.2$ porous PZT-2 skeleton containing a representative water-like pore fluid, with drained stiffness from the same RVE homogenization and the Biot–Willis coefficient $\alpha_{\mathrm{B}} = 1 - K_{\mathrm{d}}/K_{\mathrm{s}} = 0.479$, where K_{d} and K_{s} are the drained-frame and solid-grain bulk moduli. The COMSOL interface uses the drained (u, p_{f}) formulation rather than the phase-displacement (u, U) form of the present work; the two are equivalent and mutually convertible, and the conversion is not detailed here.

Figure 6 shows the wavefront patterns in the time–angle plane for the finite-element (left column) and FDTD (right column) solutions of the axial solid velocity, the transverse solid velocity, and the fluid-phase stress. Here the axial direction is the poling axis, labelled y in the finite-element model and z in the FDTD. Three arrival bands appear—the fast P wave near 1.5 μs, the quasi-shear wave near 2.3 μs, and the Biot slow wave near 3.4 μs—and all three follow the black Christoffel peak-arrival curves in both solvers. The slow wave is most distinct in the fluid-stress panel, consistent with its fluid-dominated polarization, and the FDTD panels show no spurious reflection from the truncation boundary. The two models are driven by different sources: the FDTD scheme by a time-domain velocity source, the finite-element solution by a frequency-domain force source. Both are Ricker wavelets but of different magnitude, so the field amplitudes are not directly comparable, as is evident from the differing colour-bar scales of

the two columns; the wavefront kinematics, which the comparison targets, nonetheless coincide in this low-dispersion regime.

Across the three modes and representative angles, the FDTD and finite-element arrival times agree with the Christoffel prediction to within roughly ±35 ns. The measured deviations are consistently negative: the simulated peaks arrive a few tens of nanoseconds ahead of the geometric times. This small advance is characteristic of the long-tailed two-dimensional Green's function, which shifts band-limited peaks slightly ahead of the geometric arrival, and it is an order of magnitude below the ~ 250 ns half-width of the Ricker wavelet. The agreement of three independent methods in this limit supports the three-phase scheme used in Subsections 3.2 and 3.3. This comparison addresses the non-piezoelectric two-phase limit.

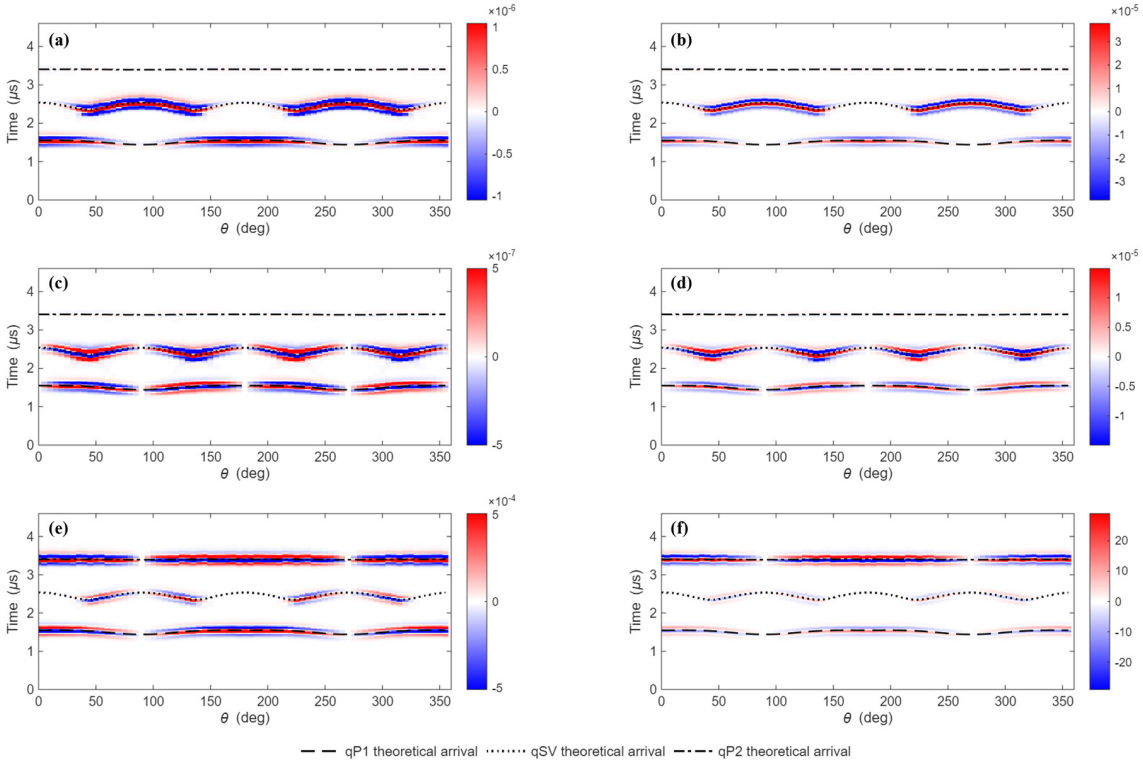


Fig. 6. (color online) Reduced non-piezoelectric poroelastic limit. Finite-element (left column: a, c, e) and FDTD (right column: b, d, f) solutions: (a, b) axial solid velocity, (c, d) transverse solid velocity, and (e, f) fluid-phase stress. The black curves mark the theoretical peak-arrival prediction.

A further comparison concerns a two-phase porous piezoelectric medium, for which published Christoffel results are available. The plane-wave problem was solved with the material parameters and calculation conditions adopted by Vashishth and Gupta [11]; the resulting slowness curves are shown in Fig. 7(a) and the published ones in Fig. 7(b). Both carry the same four branches—qP1, qP2, qSV, and SH here, P1, P2, S1, and S2 in that reference—and a closely similar angular dependence. The two quasi-compressional branches keep the same ordering and the same sense of anisotropy, while the two shear branches remain close to each other and nearly circular, separating only away from the symmetry axis.

The formulation was also examined in the isotropic, non-piezoelectric three-phase limit, with the material parameters and calculation conditions adopted by Carcione and Seriani [18]. Figure 7(c) shows the computed skeleton vertical velocity and Fig. 7(d) the published wavefield. The two display the same five wave types in the same radial order, the outer fast compressional and shear fronts enclosing the slower

P2, S2, and P3 rings. This count is the isotropic counterpart of the seven branches of Subsection 3.2: as the skeleton loses its transverse isotropy, each in-plane quasi-shear branch merges with its antiplane partner, so that qSV1 and SH1 become S1 and qSV2 and SH2 become S2. Together, these comparisons complement the finite-element benchmark by covering the two-phase porous piezoelectric and the isotropic non-piezoelectric three-phase cases.

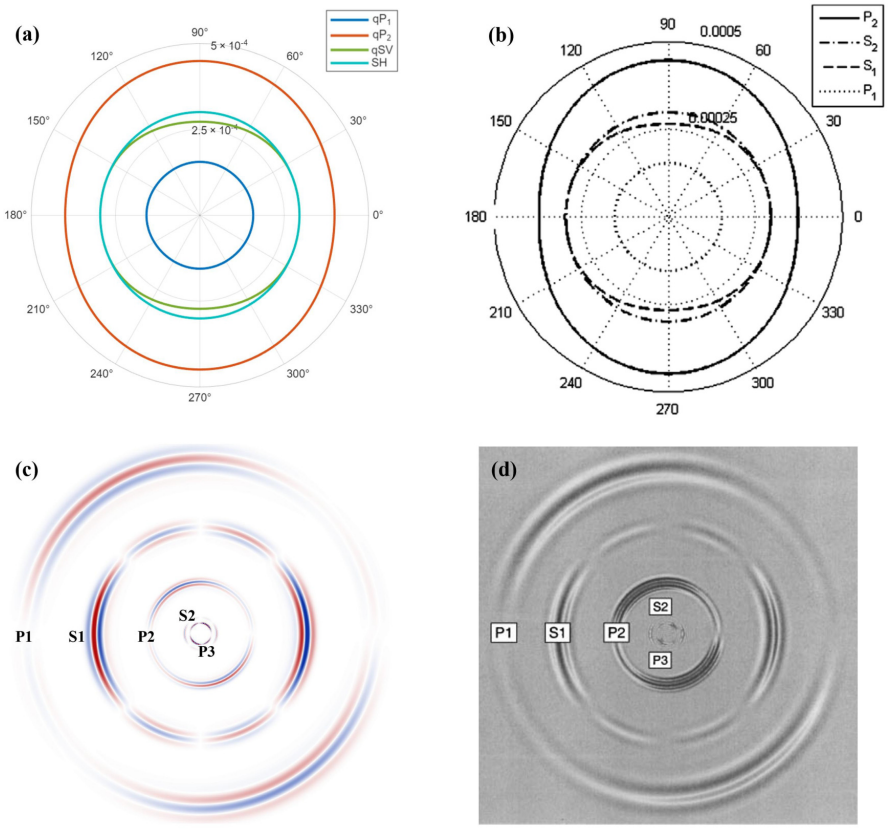


Fig. 7. (color online) Comparison with published results in two reduced cases. (a, b) Slowness curves of the four modes of a two-phase porous piezoelectric medium, the radial coordinate being the slowness (in units of $\mathrm{s \cdot m^{-1}}$): (a) present calculation and (b) the published result of Ref. [11]. (c, d) Skeleton vertical velocity in an isotropic non-piezoelectric three-phase medium: (c) present calculation and (d) the published result of Ref. [18], the two being normalized separately. Panel (b) reprinted from Ref. [11], Copyright (2009), and panel (d) from Ref. [18], Copyright (2001), with permission from Elsevier.

3.5. Effect of piezoelectric coupling

To isolate the contribution of the piezoelectric coupling, we repeat the computation with the piezoelectric coupling of the skeleton switched off ($e_{kij} = 0$) while keeping every other parameter of Table 1 fixed, and compare the result with that of the fully coupled medium. In this non-piezoelectric reference medium G drops out of Eqs. (18)–(20) and Eq. (21) becomes a separate relation for G alone, so the wave velocities follow from the mechanical 9×9 block of Eq. (22). The results show that the piezoelectric coupling stiffens the in-plane wave modes anisotropically: along the poling axis ($\theta = 0°$) the qP1 group velocity increases by 14.8%, whereas perpendicular to it ($\theta = 90°$) the qSV1 group velocity increases by 10.1% [Fig. 8(a)]. A single-constant analysis of the Christoffel solution, in which the piezoelectric constants are switched on one at a time, attributes these two effects to distinct constants: the axial stiffening of

qP1 arises almost entirely from e_{33} and the transverse stiffening of qSV1 from e_{15}, whereas e_{31} contributes negligibly in this plane.

The other in-plane modes stiffen only weakly, the qP2 and qP3 velocities rising by 1.3% and 1.6% near the axis and the qSV2 velocity by 0.4%. This change is small but nonzero, and it is physically meaningful: although piezoelectricity resides only in the skeleton, the electromechanical coupling still reaches the filling-solid and fluid-borne modes indirectly. By stiffening the skeleton, it acts through the interphase stiffness and inertial couplings that bind the three phases, so that the slow waves associated with the filling solid and the pore fluid are modified as well, even though neither the pore fluid nor the filling solid is itself piezoelectric. The two out-of-plane SH modes are the exception: governed by the antiplane block, which contains no piezoelectric or dielectric constant (Appendix A), they are strictly unchanged, and are therefore omitted from the polar diagram of Fig. 8(a), which compares the five in-plane modes for the medium with and without the coupling.

The directional stiffening is visible directly in the simulated wavefield. Figures 8(b) and 8(c) show snapshots of the skeleton vertical velocity $v_z^{(1)}$ at $t = 1.5$ μs with and without the coupling, drawn on a common colour scale. With the coupling the outer qP1 front extends noticeably farther along the poling axis (z), while its extent in the perpendicular (x) direction is essentially unchanged. This directional expansion of the wavefront mirrors the strong stiffening of qP1 along the poling axis and its near-absence perpendicular to it.

The receiver waveforms confirm the stiffening quantitatively. Figure 9 superposes the skeleton velocity $v_z^{(1)}$ recorded with and without the coupling at $\theta = 0°$, 30°, and 60°, the traces being normalized panel by panel. At $\theta = 0°$ the leading qP1 packet arrives 0.122 μs earlier with the coupling, in close agreement with the Christoffel prediction of 0.125 μs, and the same advance, though smaller, is visible at 30° and 60°. This shift is far larger than the $\sim$15 ns arrival-time accuracy established in Subsection 3.3, so the time-domain simulation independently confirms the piezoelectric stiffening obtained from the Christoffel solution. Beyond the arrival times, the coupling also redistributes the relative amplitudes of the in-plane packets. At $\theta = 30°$, for example, the leading packet is reduced and a larger share of the motion appears in the later in-plane arrivals, consistent with the coupling modifying the modal polarizations as well as the velocities.

In summary, for the three-phase porous piezoelectric medium considered here—a transversely isotropic piezoelectric skeleton sharing its pore space with a fluid and a non-piezoelectric filling solid—the piezoelectric coupling produces a strong and anisotropic stiffening of the skeleton-borne qP1 and qSV1 and a weak stiffening of the filling-solid and fluid-borne modes, while leaving the SH modes strictly unchanged. This last point reflects the 6mm symmetry of the skeleton: in the sagittal plane the SH motion belongs to the antiplane block, which is free of piezoelectric constants, and is therefore, alone among the modes, insensitive to the coupling, whereas the in-plane modes remain coupled to it. The analytical velocities establish this picture, and the time-domain FDTD results support it for the five in-plane modes through their arrival-time and amplitude behaviour.

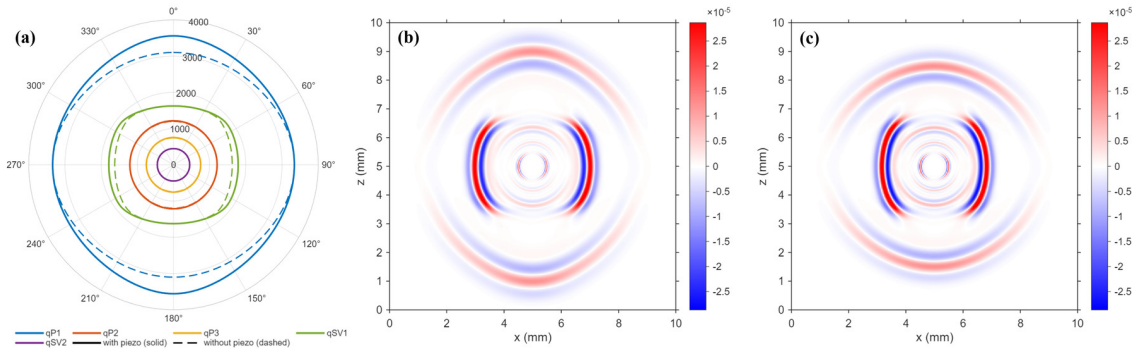


Fig. 8. (color online) Effect of piezoelectric coupling. (a) Group-velocity polar diagram of the five in-plane modes, with coupling (solid) and without (dashed). (b) Skeleton vertical velocity $v_z^{(1)}$ at $t = 1.5$ μs with coupling. (c) Skeleton vertical velocity $v_z^{(1)}$ at $t = 1.5$ μs without coupling.

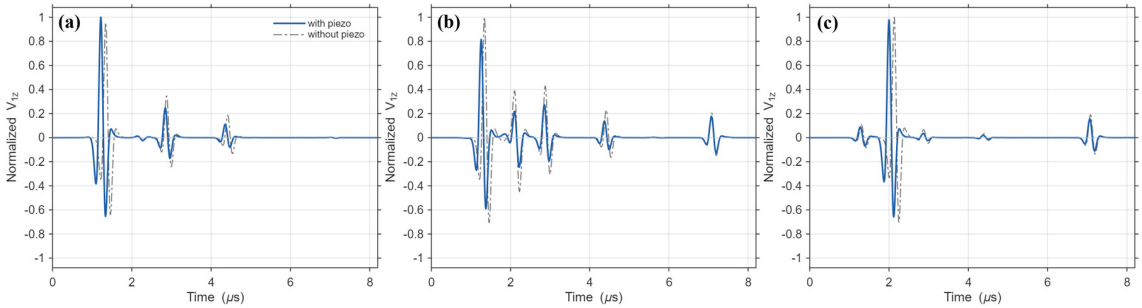


Fig. 9. (color online) Skeleton vertical velocity $v_z^{(1)}$ at propagation angles (a) $\theta = 0°$, (b) $\theta = 30°$, and (c) $\theta = 60°$. Solid curve, with coupling; dash-dotted curve, without.

3.6. Effects of interphase friction on slow-wave attenuation

The interphase friction is the only source of dissipation included in the present model. The three constituents are assigned real-valued elastic constants, so energy is lost solely when the velocity-proportional interphase-friction terms $b_{ik}^{\alpha\beta}(\dot{u}_k^{(\alpha)} - \dot{u}_k^{(\beta)})$ of the momentum equations (12)–(14) act on the *relative* motion between two phases. This friction enters the Christoffel system through the imaginary parts of the complex densities of Eq. (17), which make the velocity v complex; the attenuation is conveniently measured by the inverse quality factor $Q^{-1} = 2v_{\mathrm{p}}\alpha/\omega$, the dimensionless loss per cycle formed from the same complex root as Eq. (23). Because the friction makes the wave speed complex and frequency dependent, the group-velocity relation (24) is not applied in this subsection; the analysis rests on Q^{-1} together with the amplitude decay measured at the receivers. A mode that moves the two phases in phase, with no relative displacement, is not dissipated; this criterion determines which modes a given coefficient attenuates. This work focuses on b^{12} and b^{13}, both scalars for the isotropic pore space of Table 1. As stated in Subsection 2.2, the two coefficients are varied independently over several decades rather than set by the Darcy relation at a particular permeability; the analytical attenuation is evaluated at the 3 MHz centre frequency of the source, and the FDTD simulations use the band-limited Ricker pulse centred at that frequency. They act on different pairs of phases: the skeleton–fluid friction b^{12} damps the relative motion between the skeleton and the pore fluid, and the skeleton–infill friction b^{13} damps the relative motion between the two solids.

From the Christoffel equation, the effect of each friction coefficient on the attenuation can be evaluated at this frequency; the result is shown in Fig. 10 for $\theta = 45°$. Figure 10(a) gives the effect of the skeleton–

fluid friction b^{12}. As b^{12} increases it directly attenuates the fluid slow wave qP3, whose Q^{-1} rises steadily and then levels off at a high, nearly constant value. The qP3 wave exists only by virtue of the skeleton–fluid relative motion, and a strong b^{12} progressively suppresses that very motion, over-damping the mode into a diffusive one; its attenuation therefore stays high rather than decaying. The other modes behave in the opposite way, their Q^{-1} first rising and then falling. In the low-damping regime, increasing b^{12} dissipates more of the interphase relative motion, so the attenuation grows; in the high-damping regime, the strong friction locks the corresponding pair of phases into nearly common motion, which removes the relative motion that channel dissipates, and these truly propagating waves are again carried almost without loss, so their attenuation falls back. Figure 10(b) shows the same picture for the skeleton–infill friction b^{13}: now it is the two filling-solid waves qP2 and qSV2, sustained by the relative motion of the two solids, that remain strongly attenuated, while the remaining modes rise and then fall. Each coefficient thus over-damps only the slow modes built on the relative motion it dissipates, while the Q^{-1} of the remaining modes rises and then falls back.

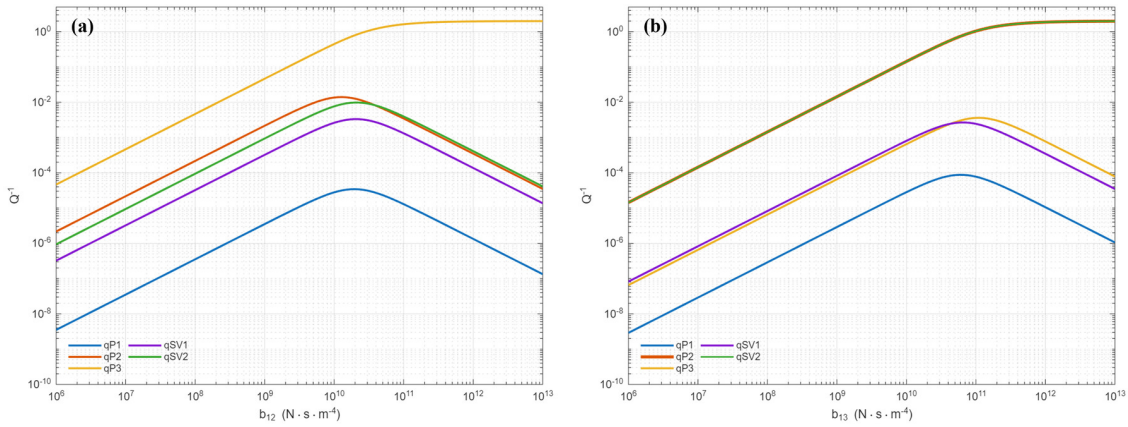


Fig. 10. (color online) Analytical attenuation Q^{-1} of the in-plane modes at $\theta = 45^\circ$ and $f = 3$ MHz: (a) versus the skeleton–fluid friction b^{12}; (b) versus the skeleton–infill friction b^{13}.

The attenuation of the slow modes is essentially independent of propagation direction. In the present medium only the piezoelectric skeleton is anisotropic, the pore fluid and the filling solid being treated as isotropic, and the friction term ib/ω is a scalar. The slow modes, dominated by the isotropic pore fluid and filling solid, therefore lose energy at nearly the same rate in every direction: from $\theta = 0^\circ$ to 90° the analytical Q^{-1} of qP3, qP2, and qSV2 varies by only a few tenths of a percent. The only modes with anisotropic attenuation are the skeleton fast waves qP1 and qSV1, but their friction-induced Q^{-1} is of order 10^{-6}, four orders of magnitude below that of the slow modes, and is negligible at the receiver. The observable slow-mode attenuation is therefore effectively isotropic, so a single propagation direction represents it faithfully.

We now examine this analytical picture using the time-domain FDTD simulation. Because the simulation must remain stable and runs only to a finite time, and because the predicted fast-wave rollover is in any case hard to observe at the receiver, the friction values used here lie mainly in the low-damping, rising branch of Fig. 10; for each coefficient we display three representative values, $b^{12} \in \{0,\ 4\times10^{8},\ 2\times10^{9}\}$ N · s · m^{-4} and $b^{13} \in \{0,\ 1.3\times10^{9},\ 5\times10^{10}\}$ N · s · m^{-4}, spanning the range from no

attenuation to near-complete suppression of the corresponding slow waves. The skeleton–fluid friction b^{12} attenuates the fluid slow wave qP3: the snapshots of the pore-fluid velocity $v_z^{(2)}$ [Fig. 11] show the inner qP3 ring weakening markedly as b^{12} increases while the outer fast fronts stay unchanged. The receiver waveforms [Fig. 12] show the qP3 packet shrinking monotonically with b^{12} until it is barely observable, and the reduction is nearly uniform over the recorded angles, in accord with the isotropy established above. The skeleton–infill friction b^{13} acts in the same way on the two filling-solid waves: the snapshots of the filling-solid velocity $v_z^{(3)}$ [Fig. 13] show the central qSV2 shear lobes and the qP2 ring weakening as b^{13} grows. The waveforms [Fig. 14] show both the qSV2 and qP2 packets diminishing monotonically with b^{13}. Throughout, the early qP1 and qSV1 arrivals are unchanged, confirming the theoretical prediction that the friction attenuation acts mainly on the slow modes, its effect on the fast skeleton waves being too small to observe at the receiver.

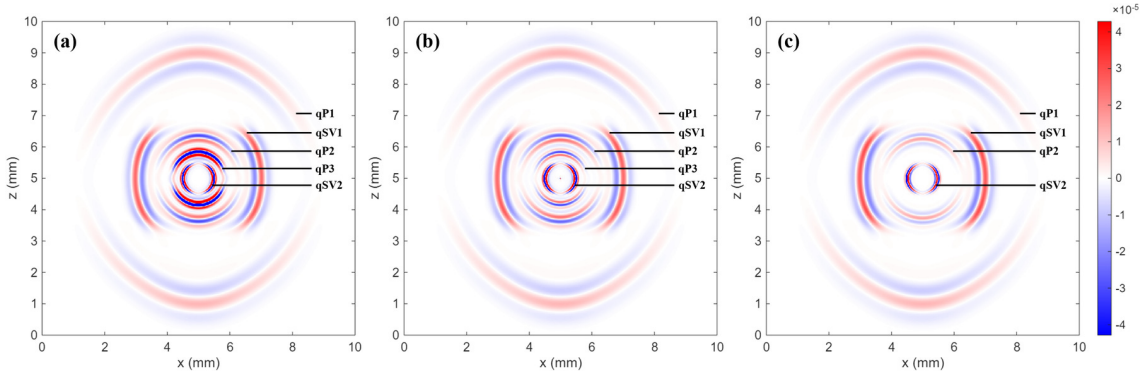


Fig. 11. (color online) Snapshots of the pore-fluid velocity $v_z^{(2)}$ at $t = 1.5\ \mu$s for three values of the skeleton–fluid friction b^{12} (in units of $\mathrm{N \cdot s \cdot m^{-4}}$): (a) 0, (b) 4×10^8, and (c) 2×10^9.

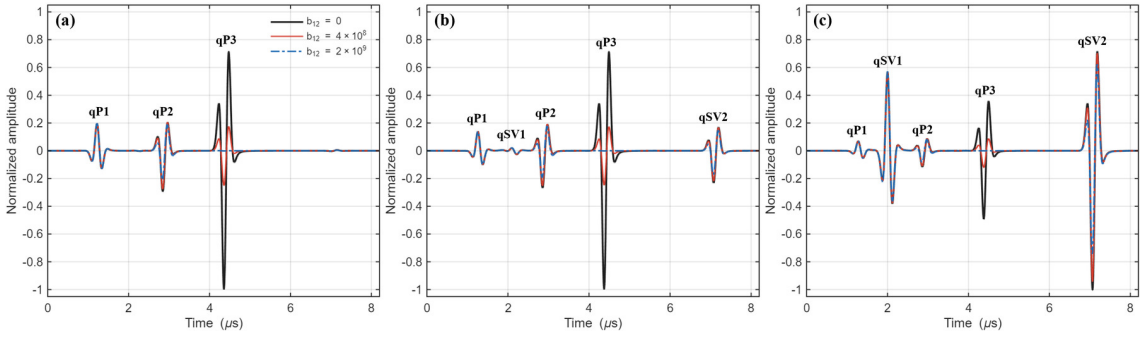


Fig. 12. (color online) Pore-fluid velocity $v_z^{(2)}$ recorded at $r_0 = 3.0$ mm for different b^{12}, at (a) $\theta = 0°$, (b) $\theta = 30°$, and (c) $\theta = 60°$.

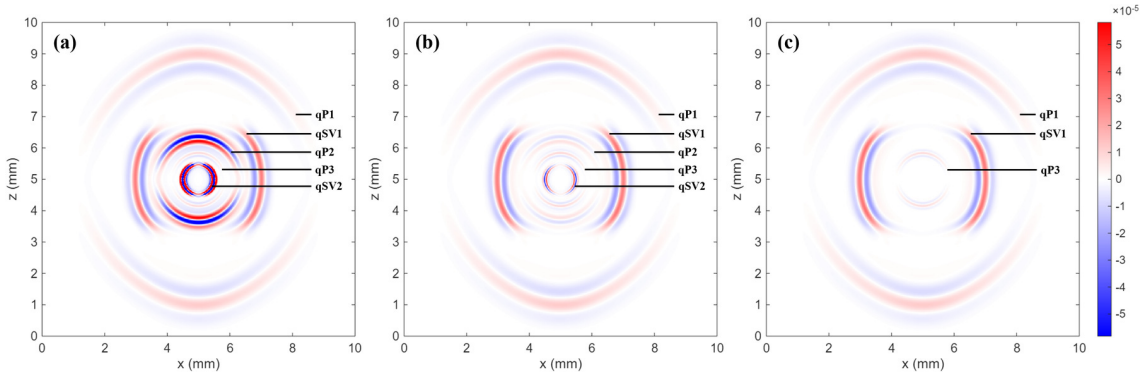


Fig. 13. (color online) Snapshots of the filling-solid velocity $v_z^{(3)}$ at $t = 1.5\ \mu$s for three values of the skeleton–infill friction b^{13} (in units of $\mathrm{N \cdot s \cdot m^{-4}}$): (a) 0, (b) 1.3×10^9, and (c) 5×10^{10}.

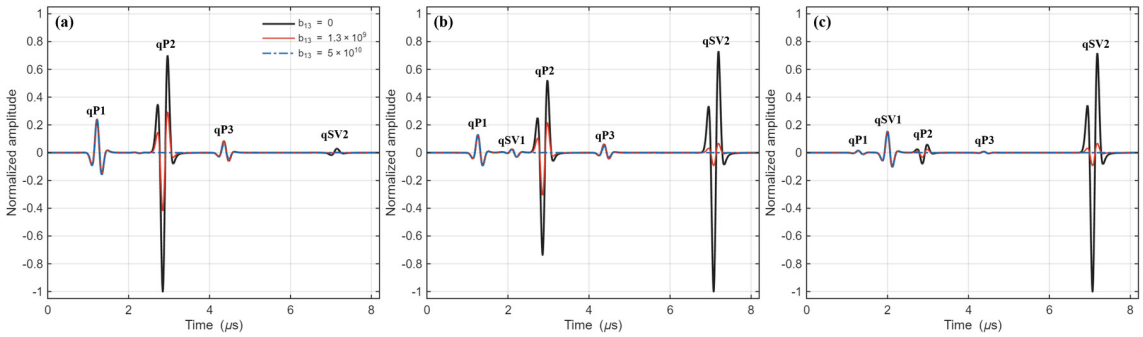


Fig. 14. (color online) Filling-solid velocity $v_z^{(3)}$ recorded at $r_0 = 3.0$ mm for different b^{13}, at (a) $\theta = 0°$, (b) $\theta = 30°$, and (c) $\theta = 60°$.

Building on this, we extend the range of b covered by the FDTD computation and compare the simulated and analytical attenuation quantitatively, as shown in Fig. 15. The analytical attenuation, expressed in percent, is $100\,(1 - \mathrm{e}^{-\alpha r_0})$, with α taken from the complex Christoffel velocity and r_0 the receiver radius; the simulated attenuation is read at the receiver array as the reduction of the peak amplitude of each slow-wave packet, isolated by a window centred on the arrival predicted by the frictionless reference group velocity, relative to its frictionless reference. The two are obtained by independent numerical routes from the same constant-friction model and carry no fitting parameter, yet qP3 against b^{12} [Fig. 15(a)] and qP2 and qSV2 against b^{13} [Fig. 15(b)] coincide point by point, from the onset of attenuation to the high-attenuation plateau. A single representative direction, $\theta = 0°$, suffices because the slow-mode attenuation is isotropic. This agreement establishes the numerical consistency of the frequency-domain and time-domain solutions of the same constant-friction model.

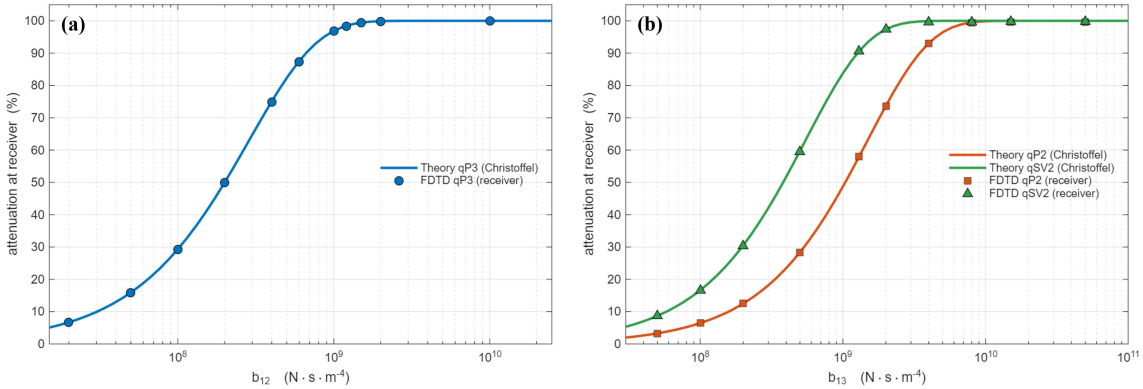


Fig. 15. (color online) Comparison of the analytical attenuation (solid curves) and the FDTD receiver attenuation (markers) at the propagation direction $\theta = 0°$; the analytical values are evaluated at $f = 3$ MHz and the simulations use a Ricker pulse centred at the same frequency: (a) qP3 versus the skeleton–fluid friction b^{12}; (b) qP2 and qSV2 versus the skeleton–infill friction b^{13}.

Two caveats should be stated. First, the fast-wave rollover of Fig. 10 is a genuine prediction but is invisible at the receiver, the corresponding amplitude change being negligible, so we make no claim of having verified it in the simulation. Second, the single source spectrum used here does not permit any conclusion about the frequency dependence of the attenuation. Within these bounds the picture is consistent with the three-phase poroelastic results of Liu *et al.* [21], in which the solid–solid friction and the fluid drag govern the slow-mode attenuation: friction renders the slow waves nearly unobservable at the array while the fast skeleton waves persist intact.

Beyond these caveats, the intrinsic losses left out of the model deserve comment. The elastic constants of the three phases and the dielectric constants of the skeleton are all taken to be real, so intrinsic mechanical damping of the skeleton, viscoelasticity of the filling solid, and dielectric loss are absent from the present formulation. Skeleton damping would mainly add attenuation to the skeleton-borne qP1, qSV1, and SH1 waves. Viscoelasticity of the filling solid would act likewise on the filling-solid-borne qP2, qSV2, and SH2. Dielectric loss would delay the electric response and perturb the piezoelectric stiffening of the in-plane modes, leaving the SH branches untouched since they generate no electric field. The attenuation reported here is therefore the isolated contribution of the interphase friction, not the total attenuation of a specific material. These mechanisms can be incorporated through complex, frequency-dependent constitutive constants and their time-domain counterparts. The same qualification applies to the fluid-related friction itself: above the characteristic frequency estimated in Subsection 3.1, a dynamic permeability would replace the constant Darcy coefficients, so the values reported in this subsection characterize the constant-friction model rather than a material-specific prediction at 3 MHz.

4. Conclusion

We have studied acoustic wave propagation in a three-phase porous piezoelectric medium consisting of a transversely isotropic (6mm) piezoelectric skeleton, a compressible pore fluid, and a non-piezoelectric filling solid, with the piezoelectric effect confined to the skeleton. Coupling the Biot-type three-phase momentum balance with the piezoelectric constitutive law gives the governing equations. A plane-wave ansatz reduces them to a complex Christoffel system that yields the phase velocity, group velocity, and attenuation of every mode. For the wavefield simulation, we developed a two-dimensional electromechanically coupled staggered-grid finite-difference time-domain scheme, terminated by a perfectly matched layer that absorbs the skeleton, fluid, and electric-potential fields together. The simulated arrival times follow the Christoffel group-velocity prediction to within 15 ns (below 1%) in all directions, and in the reduced single-solid, single-fluid limit the scheme agrees with a COMSOL poroelastic-wave solution to within ± 35 ns. The reduced results are also consistent with published two-phase porous piezoelectric and isotropic three-phase benchmarks.

Taken together, the results reveal three features of wave propagation in this medium. (i) Seven body-wave modes propagate in each direction: three quasi-compressional waves (qP1, qP2, qP3), two quasi-shear waves (qSV1, qSV2), and two horizontally polarized shear waves (SH1, SH2). The transverse isotropy of the skeleton lifts the shear degeneracy of the isotropic three-phase model, and each mode is borne predominantly by one constituent. (ii) The piezoelectric coupling stiffens the skeleton-borne modes strongly and anisotropically, raising the qP1 group velocity by 14.8% along the poling axis and the qSV1 group velocity by 10.1% perpendicular to it, traceable to e_{33} and e_{15} respectively; the filling-solid and fluid modes stiffen only weakly through the interphase couplings, while the SH modes stay strictly unchanged. (iii) Interphase friction, the only dissipation mechanism included in the present model, selectively attenuates the different slow modes: the skeleton–fluid friction b^{12} damps the fluid slow wave

qP3, whereas the skeleton–infill friction b^{13} damps the filling-solid waves qP2 and qSV2, the fast skeleton waves remaining essentially unaffected. The time-domain simulation corroborates the in-plane results: the qP1 packet arrives 0.122 μs earlier with the coupling (Christoffel: 0.125 μs), and the receiver attenuation matches the complex-velocity prediction point by point.

A few assumptions bound these results. The electric field is treated quasi-statically, and the simulation is two-dimensional and confined to the sagittal plane, so the SH waves cannot be captured by the finite-difference scheme. The effective stiffness, coupling, and electromechanical coefficients that enter the governing equations are obtained from representative-volume-element homogenization together with the closed-form three-phase poroelastic relations. The two methods also treat frequency content differently. The velocities and arrival times reported here belong to the frictionless reference state, in which the Christoffel system carries no frequency and the medium is non-dispersive, whereas the attenuation quantities are evaluated at the centre frequency of the source; no conclusion about the broadband frequency dependence of the attenuation is intended. The finite-difference scheme, in contrast, accepts an arbitrary source and returns the time-domain wavefield response under any excitation, which is closer to a practical measurement and offers a natural route to the frequency dependence of the velocities and attenuation. The theory and the coupled electromechanical simulation reported here should provide a basis for the acoustic modelling and characterization of multiphase porous piezoelectric media, with potential applications to the design of porous piezoelectric transducers and the modelling of piezoelectric biological tissues such as bone.

Appendix A: Christoffel matrix in the sagittal plane

For propagation in the sagittal plane, $n_1 = \sin\theta$, $n_2 = 0$, and $n_3 = \cos\theta$, and the 10×10 system $\boldsymbol{M}(v, \boldsymbol{n})\boldsymbol{U} = \boldsymbol{0}$ of Eq. (22) separates into a 7×7 in-plane block and a 3×3 antiplane block. Ordering the in-plane amplitudes as $(B_1, B_3, F_1, F_3, W_1, W_3, G)$, the symmetric in-plane matrix $\boldsymbol{\Gamma}$ ($\Gamma_{qp} = \Gamma_{pq}$) has

nonzero entries

$$
\begin{aligned}
\Gamma_{11} &= c_{11}^{(11)} n_1^2 + c_{44}^{(11)} n_3^2 - \bar{\rho}_{11}^{11} v^2, \quad \Gamma_{12} = (c_{13}^{(11)} + c_{44}^{(11)}) n_1 n_3, \\
\Gamma_{13} &= m_{11}^{(12)} n_1^2 - \bar{\rho}_{11}^{12} v^2, \quad \Gamma_{14} = m_{11}^{(12)} n_1 n_3, \\
\Gamma_{15} &= c_{11}^{(13)} n_1^2 + c_{44}^{(13)} n_3^2 - \bar{\rho}_{11}^{13} v^2, \quad \Gamma_{16} = (c_{13}^{(13)} + c_{44}^{(13)}) n_1 n_3, \\
\Gamma_{17} &= (e_{15} + e_{31}) n_1 n_3, \quad \Gamma_{22} = c_{44}^{(11)} n_1^2 + c_{33}^{(11)} n_3^2 - \bar{\rho}_{33}^{11} v^2, \\
\Gamma_{23} &= m_{33}^{(12)} n_1 n_3, \quad \Gamma_{24} = m_{33}^{(12)} n_3^2 - \bar{\rho}_{33}^{12} v^2, \\
\Gamma_{25} &= (c_{13}^{(13)} + c_{44}^{(13)}) n_1 n_3, \quad \Gamma_{26} = c_{44}^{(13)} n_1^2 + c_{33}^{(13)} n_3^2 - \bar{\rho}_{33}^{13} v^2, \\
\Gamma_{27} &= e_{15} n_1^2 + e_{33} n_3^2, \quad \Gamma_{33} = R n_1^2 - \bar{\rho}_{11}^{22} v^2, \\
\Gamma_{34} &= R n_1 n_3, \quad \Gamma_{35} = m_{11}^{(32)} n_1^2 - \bar{\rho}_{11}^{23} v^2, \\
\Gamma_{36} &= m_{33}^{(32)} n_1 n_3, \quad \Gamma_{44} = R n_3^2 - \bar{\rho}_{33}^{22} v^2, \\
\Gamma_{45} &= m_{11}^{(32)} n_1 n_3, \quad \Gamma_{46} = m_{33}^{(32)} n_3^2 - \bar{\rho}_{33}^{23} v^2, \\
\Gamma_{55} &= (\lambda_3 + 2\mu_3) n_1^2 + \mu_3 n_3^2 - \bar{\rho}_{11}^{33} v^2, \quad \Gamma_{56} = (\lambda_3 + \mu_3) n_1 n_3, \\
\Gamma_{66} &= \mu_3 n_1^2 + (\lambda_3 + 2\mu_3) n_3^2 - \bar{\rho}_{33}^{33} v^2, \quad \Gamma_{77} = -(\xi_{11} n_1^2 + \xi_{33} n_3^2),
\end{aligned}
\tag{A1}
$$

with $\Gamma_{37} = \Gamma_{47} = \Gamma_{57} = \Gamma_{67} = 0$. The antiplane block, ordering the amplitudes as (B_2, F_2, W_2), reads

$$
\begin{pmatrix}
c_{66}^{(11)} n_1^2 + c_{44}^{(11)} n_3^2 - \bar{\rho}_{11}^{11} v^2 & -\bar{\rho}_{11}^{12} v^2 & c_{66}^{(13)} n_1^2 + c_{44}^{(13)} n_3^2 - \bar{\rho}_{11}^{13} v^2 \\
-\bar{\rho}_{11}^{12} v^2 & -\bar{\rho}_{11}^{22} v^2 & -\bar{\rho}_{11}^{23} v^2 \\
c_{66}^{(13)} n_1^2 + c_{44}^{(13)} n_3^2 - \bar{\rho}_{11}^{13} v^2 & -\bar{\rho}_{11}^{23} v^2 & \mu_3 - \bar{\rho}_{11}^{33} v^2
\end{pmatrix}
\begin{pmatrix} B_2 \\ F_2 \\ W_2 \end{pmatrix} = \mathbf{0},
\tag{A2}
$$

with $c_{66}^{(11)} = (c_{11}^{(11)} - c_{12}^{(11)})/2$ and $c_{66}^{(13)} = (c_{11}^{(13)} - c_{12}^{(13)})/2$. The antiplane matrix involves no piezoelectric or dielectric constant, confirming that the SH motion is unaffected by the electromechanical coupling.

Appendix B: Construction of the effective coefficients

This appendix records how the coefficients of the governing equations are obtained—the elastic and coupling coefficients by construction from the entries of Table 1 and the closure relations specified below, the density matrix as a representative effective set stated in full—and verifies the positive definiteness of the assembled matrices. The volume fractions of the three phases are

$$
\phi_1 = 1 - \phi, \qquad \phi_2 = \phi(1 - S_3), \qquad \phi_3 = \phi S_3,
\tag{B1}
$$

so that $\phi_1 + \phi_2 + \phi_3 = 1$, and we write $M_\alpha = \phi_\alpha \rho^{(\alpha)}$ for the mass of phase α per unit bulk volume.

Skeleton parameter set. The frame constants A_{IJ}, the piezoelectric constants e_{iJ}, and the clamped permittivities ξ_{ij} of Table 1 describe the porous piezoelectric skeleton at $\phi = 0.4$ and are transversely isotropic about the poling axis. Their values follow a periodic-cell homogenization of the drained skeleton, carried out as follows. The cell is a cube of dense PZT-2 poled along x_3, perforated by three mutually orthogonal circular cylindrical channels that run along the coordinate axes through the cell centre and

intersect there, so that the pore space is connected in all three directions; the porosity of this geometry is $\phi = 3\pi(r/L)^2 - 8\sqrt{2}\,(r/L)^3$, with r the channel radius and L the cell edge, and $\phi = 0.4$ corresponds to $r/L = 0.245$. Periodic conditions are imposed on the displacement and on the electric potential, the cell-averaged strain and electric field are prescribed, the potential is referenced at a cell corner, and the pore space is left drained. Nine load cases—six unit average strains and three unit average electric fields—are solved, and the volume-averaged stress and electric displacement give the constant-electric-field stiffness, the piezoelectric stress constants, and the clamped permittivity of the porous skeleton [16]. Refining the mesh changes these constants by less than 0.2%. The grain bulk modulus K_{s1} of Table 1 is the Voigt average of the stiffness of dense PZT-2.

Volumetric coupling coefficients. The bulk modulus of the drained skeleton frame is the Voigt projection of A_{IJ},

$$K_{\mathrm{m1}} = \tfrac{1}{9}\big[2(A_{11} + A_{12}) + 4A_{13} + A_{33}\big], \tag{B2}$$

while the frame moduli of the filling solid follow a percolation-type relation [17,39], in which we identify the modulus of the fully connected end-member with the modulus of the constituent,

$$K_{\mathrm{m3}} = K_{\mathrm{s3}} S_3^{\,n}, \qquad \mu_{\mathrm{m3}} = \mu_{\mathrm{s3}} S_3^{\,n}, \tag{B3}$$

with the exponent n of Table 1. The consolidation coefficients of the two solid frames and the average modulus of the aggregate are [17,39]

$$c_1 = \frac{K_{\mathrm{m1}}}{\phi_1 K_{\mathrm{s1}}}, \qquad c_3 = \frac{K_{\mathrm{m3}}}{\phi_3 K_{\mathrm{s3}}}, \qquad K_{\mathrm{av}} = \left[\frac{(1-c_1)\phi_1}{K_{\mathrm{s1}}} + \frac{\phi_2}{K_{\mathrm{f}}} + \frac{(1-c_3)\phi_3}{K_{\mathrm{s3}}}\right]^{-1}, \tag{B4}$$

from which the volumetric coupling coefficients follow in closed form [18,39,40],

$$\begin{aligned} R &= \phi_2^2 K_{\mathrm{av}}, \qquad C_{12} = (1-c_1)\phi_1\phi_2 K_{\mathrm{av}}, \\ C_{23} &= (1-c_3)\phi_3\phi_2 K_{\mathrm{av}}, \qquad C_{13} = (1-c_1)(1-c_3)\phi_1\phi_3 K_{\mathrm{av}}. \end{aligned} \tag{B5}$$

Equations (B3)–(B5) are those of the scalar three-phase theory. Because the anisotropy of the present medium is carried by the piezoelectric skeleton alone, we extend the scalar solid–fluid couplings to spatially isotropic tensors,

$$m_{ij}^{(12)} = C_{12}\,\delta_{ij}, \qquad m_{ij}^{(32)} = C_{23}\,\delta_{ij}. \tag{B6}$$

Stiffness tensors. For the skeleton we adopt the anisotropic counterpart of the corresponding scalar relation, in which the drained frame is augmented by the fluid coupling,

$$c_{ijkl}^{(11)} = A_{ijkl} + \frac{m_{ij}^{(12)} m_{kl}^{(12)}}{R}; \tag{B7}$$

this adds C_{12}^2/R to the normal-strain block and leaves the shear constants unchanged, and its bulk part returns the scalar result $K_1 = K_{\mathrm{m1}} + [(1-c_1)\phi_1]^2 K_{\mathrm{av}}$ of Ref. [17]. For the solid–solid coupling we adopt the closure

$$c_{IJ}^{(13)} = \chi_{13}\,A_{IJ}, \qquad \chi_{13} = \frac{C_{13}}{K_{\mathrm{m1}}}, \tag{B8}$$

which distributes the closed-form coupling C_{13} over the skeleton frame and whose bulk part returns C_{13} exactly. The filling solid is isotropic, with

$$K_3 = \big[(1-c_3)\phi_3\big]^2 K_{\mathrm{av}} + K_{\mathrm{m3}}, \qquad \mu_3 = \mu_{\mathrm{m3}}, \qquad \lambda_3 = K_3 - \tfrac{2}{3}\mu_3, \tag{B9}$$

so that $c_{11}^{(33)} = \lambda_3 + 2\mu_3$, $c_{13}^{(33)} = \lambda_3$, and $c_{44}^{(33)} = \mu_3$, as used in Subsection 2.3. No elastic shear coupling between the two solids through the fluid is retained: the pore fluid has no equilibrium shear modulus, and its viscosity enters separately through the interphase-friction terms.

Density matrix. The mass coefficients of the three-phase kinetic energy (9) are those of the Leclaire–Carcione theory [18,39,40],

$$\begin{aligned}
\rho^{11} &= a_{13}M_1 + (a_{12}-1)M_2 + (a_{31}-1)M_3, \qquad \rho^{12} = -(a_{12}-1)M_2,\\
\rho^{22} &= (a_{12}+a_{23}-1)M_2, \qquad \rho^{13} = -(a_{13}-1)M_1 - (a_{31}-1)M_3,\\
\rho^{33} &= a_{31}M_3 + (a_{23}-1)M_2 + (a_{13}-1)M_1, \qquad \rho^{23} = -(a_{23}-1)M_2,
\end{aligned} \tag{B10}$$

where a_{12} and a_{23} are the tortuosities of the fluid flowing through the skeleton and through the filling solid, and a_{13} and a_{31} describe the mutual entrainment of the two solid phases. A general parameterization of these tortuosities is given in Refs. [18,39],

$$a_{12} = 1 + r_{12}\frac{\phi_1\rho_{\mathrm{mix}}^{(23)}}{\phi_2\rho^{(2)}}, \quad a_{23} = 1 + r_{23}\frac{\phi_3\rho_{\mathrm{mix}}^{(12)}}{\phi_2\rho^{(2)}}, \quad a_{13} = 1 + r_{13}\frac{\phi_3\rho_{\mathrm{mix}}^{(13)}}{\phi_1\rho^{(1)}}, \quad a_{31} = 1 + r_{31}\frac{\phi_1\rho_{\mathrm{mix}}^{(13)}}{\phi_3\rho^{(3)}}, \tag{B11}$$

with the pairwise mixture densities

$$\rho_{\mathrm{mix}}^{(\alpha\beta)} = \frac{\phi_\alpha\rho^{(\alpha)} + \phi_\beta\rho^{(\beta)}}{\phi_\alpha + \phi_\beta}. \tag{B12}$$

The factors $r_{\alpha\beta}$ characterize the geometrical features of the interfaces between the corresponding pair of phases; they are geometry-dependent closure parameters rather than universal material constants, and the physically admissible range is $a_{\alpha\beta} \geq 1$, the value unity corresponding to phases whose micro- and macro-velocity fields coincide. The elastic closure above is fixed by the constituent moduli and the volume fractions alone, whereas this inertial closure calls for interface-geometry parameters that the constituent data do not by themselves fix. We therefore do not identify the $r_{\alpha\beta}$ from a particular pore geometry, and instead state in full the representative density matrix used in every computation of Section 3. Taking the inertia to be isotropic in space, $\rho_{ik}^{\alpha\beta} = \rho^{\alpha\beta}\delta_{ik}$, its coefficients are

$$\big[\rho^{\alpha\beta}\big] = \begin{pmatrix} 6284 & -300 & -1424 \\ -300 & 560 & -140 \\ -1424 & -140 & 1900 \end{pmatrix} \ \mathrm{kg/m^3}. \tag{B13}$$

The friction coefficients do not enter the kinetic energy and are prescribed separately (Subsections 2.2 and 3.1).

Positive definiteness. Equations (B10) can be rearranged into the pairwise form

$$K = \tfrac{1}{2}\sum_{\alpha=1}^{3} M_\alpha\big|\dot{\boldsymbol{u}}^{(\alpha)}\big|^2 + \tfrac{1}{2}\sum_{(\alpha,\beta)} q_{\alpha\beta}\big|\dot{\boldsymbol{u}}^{(\alpha)} - \dot{\boldsymbol{u}}^{(\beta)}\big|^2, \tag{B14}$$

with $q_{12} = (a_{12} - 1)M_2$, $q_{23} = (a_{23} - 1)M_2$, and $q_{13} = (a_{13} - 1)M_1 + (a_{31} - 1)M_3$. Since $M_\alpha > 0$ for all three phases and $a_{\alpha\beta} \geq 1$ implies $q_{\alpha\beta} \geq 0$, the kinetic energy is strictly positive for every nonzero velocity triplet; the generalized density matrix is therefore positive definite for any admissible set of tortuosities, and each of its rows sums to the corresponding phase mass M_α. For the matrix of Eq. (B13) the pairwise coefficients are $q_{12} = 300$, $q_{13} = 1424$, and $q_{23} = 140\ \mathrm{kg/m^3}$, all positive, and the rows return $M_1 = 4560$, $M_2 = 120$, and $M_3 = 336\ \mathrm{kg/m^3}$: the negative off-diagonal entries are thus not negative masses but the inertial coupling terms of Eq. (B14). For the elastic part, the strain energy of Eq. (3) at fixed electric field is a quadratic form in the thirteen kinematic variables $(\varepsilon_{11}^{(1)}, \varepsilon_{22}^{(1)}, \varepsilon_{33}^{(1)}, 2\varepsilon_{23}^{(1)}, 2\varepsilon_{13}^{(1)}, 2\varepsilon_{12}^{(1)}, \zeta, \varepsilon_{11}^{(3)}, \ldots, 2\varepsilon_{12}^{(3)})$, assembled from $c^{(11)}$, $c^{(13)}$, $c^{(33)}$, R, $m^{(12)}$, and $m^{(32)}$. With the parameters of Table 1 the smallest eigenvalue of this assembled mechanical matrix is 0.31 GPa, confirming its positive definiteness. The principal values of the clamped permittivity tensor are positive as well.

Appendix C: Numerical stability and convergence

For the medium of Table 1 the two bounds of Subsection 2.3 evaluate as follows. Scanning the Christoffel solution over all propagation directions gives $v_{\max} = 3557$ m/s, the axial qP1 velocity of the piezoelectrically stiffened medium, so that Eq. (31) reads $\Delta t \leq 1.93$ ns at $h = 12.5\ \mu$m, with $S = 1.286$. The friction bound is tightest for the largest coefficient used in this work, $b^{13} = 5 \times 10^{10}\ \mathrm{N{\cdot}s{\cdot}m^{-4}}$ of Subsection 3.6, for which $\lambda_{\max} = 2.72 \times 10^7\ \mathrm{s^{-1}}$ and Eq. (33) gives $\Delta t \leq 73.5$ ns. The step $\Delta t = 0.1$ ns used throughout meets the two bounds with margins of about 19 and 735.

The convergence tests use the same medium with the piezoelectric coupling active and $b^{12} = b^{13} = b^{23} = 0$. To keep the finest grid tractable they are run on a reduced square domain of 6 mm side, with the perfectly matched layer held at a fixed physical thickness of 1.0 mm and the receivers 1.5 mm from the source; the discretization, material, source and absorbing layer are otherwise those of Section 3. The source adds to the skeleton vertical velocity at a single node, so the recorded amplitude scales with the discretization; all comparisons therefore use peak arrival times and normalised waveforms $\hat{u} = u/\|u\|_2$ rather than absolute amplitudes. At the 0° and 45° receivers two windows are compared, one centred on the skeleton packet in $v_z^{(1)}$ and one on the filling-solid packet in $v_z^{(3)}$.

Table C1 collects the results, each block being measured against its own reference run (last row); $|\Delta t_{\mathrm{p}}|$ is the largest peak-arrival difference and E_2 the largest normalised-waveform error over the two windows. Halving the grid spacing at fixed Courant number and halving the time step both bring the solution closer to its reference, the largest peak-arrival difference falling from 0.36 to 0.07 ns and from 0.22 to 0.13 ns respectively, with normalised waveform errors below 2.3×10^{-3} throughout. Lowering the spatial order from eight to four leaves the two solutions close in absolute terms, with arrival-time differences below 0.21 ns and a maximum windowed waveform difference of 1.4×10^{-3}. At the setting used in Section 3 ($h = 12.5\ \mu$m, $\Delta t = 0.1$ ns, eighth order) the arrival times and normalised waveforms differ from their refined references by no more than 0.13 ns and 5.8×10^{-4} respectively; this is negligible against the maximum arrival-time deviation of 15 ns between theory and simulation reported in Subsection 3.3.

Since the grid refinement holds the Courant number fixed and therefore changes the spatial and temporal errors together, we report the differences themselves rather than a fitted convergence rate.

The explicitly integrated friction was examined by a stress test at the largest friction of this work, $b^{13} = 5 \times 10^{10}$ N·s·m^{-4} with the other two coefficients set to zero, run to 2.0 μs. The domain maxima of all six velocity components remain bounded and show no sustained growth once the source has ended, the fitted slope of their base-ten logarithm lying between -0.16 and -0.23 per microsecond. This is a numerical check over a finite time interval, not a proof of stability. Finally, repeating the coarsest case on a 10 mm domain changes the reported metrics by less than 7.6×10^{-4} in the normalised-waveform metric and 0.01 ns in peak arrival time, so the reduced domain does not affect the comparison.

Table C1. Convergence of the in-plane scheme.

h/μm	Δt/ns	order	$\lvert\Delta t_{\mathrm{p}}\rvert$/ns	E_2
(a) grid refinement at fixed Courant number				
25.00	0.20	8	0.36	2.3×10^{-3}
12.50	0.10	8	0.07	4.4×10^{-4}
6.25	0.05	8	reference	reference
(b) time-step refinement				
12.50	0.20	8	0.22	1.8×10^{-3}
12.50	0.10	8	0.13	5.8×10^{-4}
12.50	0.05	8	reference	reference
(c) spatial difference order				
12.50	0.10	4	0.21	1.4×10^{-3}
12.50	0.10	8	reference	reference

Appendix D: Quantitative performance of the absorbing layer

This appendix reports the numerical reflection coefficient defined in Eq. (36). The tests use the eighth-order staggered-grid discretization of Subsection 2.3, with $\Delta x = \Delta z = 12.5$ μm and $\Delta t = 0.1$ ns. A compact point source of nominal frequency f acts on the skeleton velocity at 1.5 mm from the inner interface of the absorbing layer, and the receivers lie inside the main domain at 0.4 mm from that interface. The nominal incidence angle follows from the source–boundary–receiver geometry and is measured with respect to the boundary normal; the receiver positions realize the angles 0°, 30°, and 45° to within 0.1°. The reference solution is computed on an enlarged grid without an absorbing layer, its outer boundary placed far enough from the receivers to exclude mechanical boundary returns within the analysis window.

Table D1 collects the results. The reflection decreases monotonically as the layer is thickened: at $f = 3.0$ MHz, increasing N_{PML} from 20 to 80, that is L_{PML} from 0.25 to 1.00 mm, lowers R_{dB} by 9.3 to 15.6 dB depending on the incidence angle. For $N_{\mathrm{PML}} = 80$, R_{dB} lies between -46.4 and -32.1 dB over the whole range tested, 1.5 to 4.5 MHz and 0° to 45°, and reaches -42.0 dB at 3.0 MHz and normal incidence, so that the maximum relative reflection error stays below 3% throughout. The reflection is consistently higher at the largest angle tested, indicating reduced absorption under oblique incidence.

Table D1. Numerical reflection coefficient of the coupled electromechanical perfectly matched layer, evaluated from Eq. (36).

N_{PML}	L_{PML}/mm	f/MHz	$R_{\mathrm{dB}}(0^\circ)$/dB	$R_{\mathrm{dB}}(30^\circ)$/dB	$R_{\mathrm{dB}}(45^\circ)$/dB
(a) dependence on layer thickness					
20	0.25	3.0	−26.50	−27.19	−26.09
40	0.50	3.0	−33.40	−34.68	−30.22
80	1.00	3.0	−42.00	−42.82	−35.36
(b) dependence on nominal source frequency					
80	1.00	1.5	−40.53	−39.19	−32.08
80	1.00	3.0	−42.00	−42.82	−35.36
80	1.00	4.5	−44.78	−46.36	−39.05

Acknowledgment

Project supported by the National Natural Science Foundation of China (Grant Nos. 12274432, 52227901, and 42127807).

References

[1] Mercadelli E and Galassi C 2021 *IEEE Trans. Ultrason. Ferroelectr. Freq. Control* **68** 217

[2] Akdoğan E K, Allahverdi M and Safari A 2005 *IEEE Trans. Ultrason. Ferroelectr. Freq. Control* **52** 746

[3] Marselli S, Pavia V, Galassi C, Roncari E, Craciun F and Guidarelli G 1999 *J. Acoust. Soc. Am.* **106** 733

[4] Tran T N H T, Le L H and Ta D 2022 *IEEE Trans. Ultrason. Ferroelectr. Freq. Control* **69** 2875

[5] Zaszczyńska A, Zabielski K, Gradys A, Kowalczyk T and Sajkiewicz P 2024 *Polymers* **16** 2797

[6] Biot M A 1956 *J. Acoust. Soc. Am.* **28** 168

[7] Biot M A 1956 *J. Acoust. Soc. Am.* **28** 179

[8] Biot M A 1962 *J. Appl. Phys.* **33** 1482

[9] Plona T J 1980 *Appl. Phys. Lett.* **36** 259

[10] Carcione J M 2022 *Wave Fields in Real Media: Wave Propagation in Anisotropic, Anelastic, Porous and Electromagnetic Media* (4th edn.) (Amsterdam: Elsevier)

[11] Vashishth A K and Gupta V 2009 *Int. J. Solids Struct.* **46** 3620

[12] Sharma M D 2010 *Proc. R. Soc. A* **466** 1977

[13] Vashishth A K and Gupta V 2014 *Proc. R. Soc. A* **470** 20140172

[14] Vashishth A K and Gupta V 2011 *J. Acoust. Soc. Am.* **129** 3690

[15] Vashishth A K and Bareja U 2023 *Eur. J. Mech. A/Solids* **99** 104908

[16] Rohan E and Lukeš V 2018 *Int. J. Solids Struct.* **147** 110

[17] Leclaire P, Cohen-Ténoudji F and Aguirre-Puente J 1994 *J. Acoust. Soc. Am.* **96** 3753

[18] Carcione J M and Seriani G 2001 *J. Comput. Phys.* **170** 676

[19] Carcione J M, Santos J E, Ravazzoli C L and Helle H B 2003 *J. Appl. Phys.* **94** 7839

[20] Guerin G and Goldberg D 2005 *Geochem. Geophys. Geosyst.* **6** Q07010

[21] Liu L, Zhang X M and Wang X M 2021 *Chin. Phys. B* **30** 024301

[22] Liu L, Zhang X M, Wang X M, He X and Chen H 2023 *Sci. Rep.* **13** 7646

[23] Liu L, Zhang X M and Wang X M 2025 *Chin. Phys. B* **34** 024301

[24] Virieux J 1986 *Geophysics* **51** 889

[25] Zeng Y Q and Liu Q H 2001 *J. Acoust. Soc. Am.* **109** 2571

[26] Rahman S, Langtangen H P and Barnes C H W 2007 *Commun. Comput. Phys.* **2** 271

[27] Chagla F and Smith P M 2006 *IEEE Trans. Ultrason. Ferroelectr. Freq. Control* **53** 1895

[28] Filoux E, Callé S, Certon D, Lethiecq M and Levassort F 2008 *J. Acoust. Soc. Am.* **123** 4165

[29] Berenger J P 1994 *J. Comput. Phys.* **114** 185

[30] Collino F and Tsogka C 2001 *Geophysics* **66** 294

[31] Zeng Y Q, He J Q and Liu Q H 2001 *Geophysics* **66** 1258

[32] Guha S and Singh A K 2022 *Finite Elem. Anal. Des.* **209** 103814

[33] Tiersten H F 1969 *Linear Piezoelectric Plate Vibrations* (New York: Plenum Press)

[34] IEEE 1988 *IEEE Standard on Piezoelectricity* ANSI/IEEE Std 176-1987 (New York: IEEE)

[35] Yang J 2005 *An Introduction to the Theory of Piezoelectricity* (New York: Springer)

[36] Johnson D L, Koplik J and Dashen R 1987 *J. Fluid Mech.* **176** 379

[37] Komatitsch D and Martin R 2007 *Geophysics* **72** SM155

[38] Martin R, Komatitsch D and Ezziani A 2008 *Geophysics* **73** T51

[39] Liu L, Zhang X M and Wang X M 2022 *J. Theor. Comput. Acoust.* **30** 2150002

[40] Carcione J M and Tinivella U 2000 *Geophysics* **65** 54